

Acceleration Feedback Control for Small Fixed-Wing UAS

by

Angela C. Maio

B.S., University of Maryland, College Park, 2016

A thesis submitted to the
Faculty of the Graduate School of the
University of Colorado in partial fulfillment
of the requirements for the degree of
Master of Science
Department of Mechanical Engineering

2018

This thesis entitled:
Acceleration Feedback Control for Small Fixed-Wing UAS
written by Angela C. Maio
has been approved for the Department of Mechanical Engineering

Prof. J. Sean Humbert

Prof. Eric W. Frew

Prof. Robert B. MacCurdy

Date _____

The final copy of this thesis has been examined by the signatories, and we find that both the content and the form meet acceptable presentation standards of scholarly work in the above mentioned discipline.

Maio, Angela C. (M.S., Mechanical Engineering)

Acceleration Feedback Control for Small Fixed-Wing UAS

Thesis directed by Prof. J. Sean Humbert

Rejection of external disturbances is crucial for small aircraft flying in environments with dynamic flow fields, especially due to their increased sensitivity to disturbances. Fixed-wing vehicles are generally controlled using successive closure of position and velocity state feedback loops. The successive loop closure method ignores aerodynamic coupling and fails in the presence of strong gusts or aircraft damage. Existing multi-input, multi-output (MIMO) control methods may include aerodynamic coupling and provide more robust performance, but still respond slowly to high speed gusts because they feed back lower order states such as position and velocity. This study aims to develop a MIMO control methodology to feed back translational and rotational acceleration states on a simulated fixed-wing aircraft, enabling quicker rejection of disturbances. The acceleration states are linearly estimated using measurements from 12 simulated uniaxial accelerometers distributed away from the center of gravity of the vehicle. The novelty of this research is in using these acceleration states in inner feedback loops in addition to the existing autopilot to demonstrate disturbance rejection on a fixed-wing vehicle before propagation to lower order states. Using the Ttwistor small Unmanned Aircraft System (sUAS) model and robust control analysis tools, a nonlinear flight simulation with and without acceleration estimation and feedback was conducted to quantify the improvement in disturbance rejection. The resulting augmented autopilot enables the small fixed-wing UAS to fly through turbulent, gusty environments by improving disturbance rejection up to 58% in some aircraft states. We also developed a framework for analyzing bare airframes as candidates for augmented control based on gust sensitivity and maneuverability. The results shown with the Ttwistor model demonstrate the limitations of this control approach on fixed-wing vehicles as well as the potential for even better gust rejection on smaller and more responsive platforms.

Acknowledgements

The author would like to express gratitude to her advisor, Professor Sean Humbert, for his research guidance and patience through one-on-one controls lessons. She also thanks Professors Eric Frew and Robert MacCurdy for their feedback and challenging questions regarding this research. The author acknowledges her colleagues at CU and ARL, especially Cosima, Badri, and Greg, for their advice and support through the inevitable blockades against research progress. Many thanks are due also to the friends and family who encouraged her to start her biggest adventure yet by moving across the country, and to all of the new friends and family that made Colorado feel like home.

The author also thanks the Logistics Management Institute (LMI) for funding her education through the SMART Scholarship for Service Program, and the U.S. Air Force Center of Excellence for funding this project through the Nature Inspired Flight Technology Ideas (NIFTI) program, Grant FA9550-14-1-0398.

Contents

Chapter	
1	1
Introduction	1
1.1	1
Motivation	1
1.2	5
Current Work	5
1.3	6
Research Contributions	6
1.4	7
Organization	7
2	8
Model Structure	8
2.1	8
Overview	8
2.2	10
Aircraft Model	10
2.2.1	10
Nonlinear Model	10
2.2.2	15
Linear Model	15
2.3	17
Disturbance/Environment Model	17
2.4	21
Conclusions	21
3	23
Assessment of Aircraft Candidacy for Augmented Control	23
3.1	23
Overview	23
3.2	23
Maneuverability	23
3.3	27
Disturbance Sensitivity	27
3.4	28
Conclusions	28

4	Control Design	33
4.1	Overview	33
4.2	Outer Loop Controller	33
4.3	Inner Loop Acceleration Feedback	35
4.4	Distributed Acceleration Sensing	36
4.5	Conclusions	41
5	Performance Analysis	43
5.1	Overview	43
5.2	Disturbance Rejection	43
5.3	Noise Sensitivity	54
5.4	Conclusions	56
6	Summary and Future Work	58
6.1	Summary	58
6.2	Future Work	59
	Bibliography	61

Tables

Table

2.1	Ttwistor aircraft geometry and mass properties.	11
2.2	Ttwistor aircraft trim state and control inputs.	15
2.3	Ttwistor aircraft linear model parameters.	18
3.1	Frobenius norms of scaled maneuverability gramians for the Ttwistor and Skywalker.	26
3.2	Frobenius norms of scaled disturbance sensitivity gramians for the Ttwistor and Skywalker.	28
5.1	Nominal and acceleration feedback performance of wind disturbance rejection.	53

Figures

Figure

1.1	Fixed-wing aircraft such as this Ttwistor aircraft can be subjected to high winds while collecting weather data near a tornado.	2
1.2	Basic outline of sensing, actuation, and control in a fly, including the halteres and campaniform sensilla which are used to measure forces and moments.	3
1.3	Scanning electron microscope images of a representative subset of fly halteres, showing large variations in shape (adapted from [5]).	4
1.4	A quadrotor with distributed accelerometers (circled in blue) and force-adaptive feedback implementation (adapted from [23]).	5
1.5	CU Boulder’s Ttwistor aircraft in flight.	6
2.1	Simulink main block diagram for the nonlinear simulation.	9
2.2	Ttwistor aircraft being launched.	10
2.3	Open loop nonlinear model structure.	11
2.4	Simulink block diagram for the aircraft model subsystem, with force and moment calculations and 6 degree-of-freedom equations of motion.	12
2.5	Open loop state space model.	16
2.6	Simulink block diagram for modeling three types of wind, Dryden turbulence, discrete gusts, and wind shear.	19
2.7	Model for Dryden wind turbulence with forming filters.	20

2.8	Dryden turbulence forming filter magnitudes for translational (top) and rotational (bottom) velocities.	22
3.1	Maneuverability ellipses for the Ttwistor open loop aircraft model.	30
3.2	Comparison of maneuverability ellipses for the Ttwistor and Skywalker open loop aircraft models.	31
3.3	Comparison of disturbance sensitivity ellipses for the Ttwistor and Skywalker open loop aircraft models.	32
4.1	Nominal LQR control model.	34
4.2	Augmented control with acceleration feedback.	36
4.3	Coordinate frames for the acceleration of a point P on the rigid body O' with respect to the inertial frame O (reproduced from [23]).	37
4.4	Modeled locations of the 4 triaxial accelerometers used for simulation, which are on the surface of a 10cm-radius sphere.	42
5.1	Sensitivity singular values for both controllers, in lateral (top) and longitudinal (bottom) directions.	45
5.2	Simulated Dryden wind velocities.	48
5.3	Time histories of longitudinal states from nonlinear simulations with each controller, for (a) 1 simulation and (b) shaded ranges for 100 simulations.	49
5.4	Time histories of lateral states from nonlinear simulations with each controller, for (a) 1 simulation and (b) shaded ranges for 100 simulations.	50
5.5	Time histories of acceleration states from nonlinear simulations with each controller, for (a) 1 simulation and (b) shaded ranges for 100 simulations.	51
5.6	Time histories of control inputs from nonlinear simulations with each controller, for (a) 1 simulation and (b) shaded ranges for 100 simulations.	52

5.7	Trajectories of the aircraft with each controller, compared to straight trim trajectory, for (a) 1 simulation and (b) 100 simulations.	54
5.8	Acceleration feedback control block diagram with additive sensor noise at the acceleration states.	55
5.9	Noise rejection singular values for the acceleration feedback controller, in longitudinal (solid) and lateral (dashed) directions.	56

Nomenclature

α	Angle of attack, rad
$\bar{\sigma}$	Maximum singular values
β	Sideslip angle, rad
β_i	Elevation angle of the i^{th} accelerometer, rad
δ_a	Aileron control input, rad
δ_e	Elevator control input, rad
δ_r	Rudder control input, rad
δ_t	Throttle control input, fraction of full-throttle from 0 to 1
γ_i	Azimuth angle of the i^{th} accelerometer, rad
\hat{e}_i	Orientation vector of the i^{th} accelerometer
\hat{x}_a	Estimated acceleration state vector
κ_i	Scale factor of the i^{th} accelerometer
ϕ	Roll Euler angle, rad
ψ	Yaw Euler angle, rad
ρ	Density of air kg/m ³
σ	Dryden turbulence intensity, m/s
$\sigma(e)$	Standard deviation of error
θ	Pitch Euler angle, rad
ε_c	Reachability ellipsoid for aircraft controllability
ε_d	Reachability ellipsoid for aircraft disturbance sensitivity
$\vec{\omega}$	Angular acceleration vector, rad/s ²
$\vec{\omega}$	Angular velocity vector, rad/s
$\vec{\omega}_B$	Aircraft angular velocity vector in body coordinates, rad/s
$\vec{\omega}_{wind}$	Angular wind velocity vector, rad/s
\vec{a}	Translational acceleration vector, m/s ²
\vec{b}	Accelerometer bias vector
\vec{d}	Disturbance vector
\vec{F}	Force vector, N

\vec{M}	Moment vector, N
\vec{n}	Acceleration noise vector
\vec{r}_i	Position vector of the i^{th} accelerometer with respect to the aircraft center of mass, m
\vec{u}	Control input vector
\vec{u}_o	Outer-loop actuator command vector
\vec{v}	Translational velocity vector, m/s
\vec{V}^E	Aircraft inertial velocity vector in body coordinates, m/s
\vec{V}_B	Air relative velocity vector in body coordinates, m/s
\vec{V}_{wind}	Translational wind velocity vector, m/s
\vec{x}	State vector
\vec{x}_a	Acceleration state vector
\vec{x}_a^E	Inertial acceleration state vector
\vec{y}	Output vector
\vec{z}	Accelerometer measurement vector
A	Dynamic state space matrix
B	Control authority state space matrix
b	Aircraft wingspan, m
C	Output state space matrix
c	Aircraft mean chord length, m
C_a	Accelerometer measurement matrix
C_D	Nonlinear drag model
C_L	Nonlinear lift model
C_l	Linear approximation of rolling moment coefficient
C_m	Linear approximation of pitching moment coefficient
C_n	Linear approximation of yawing moment coefficient
C_T	Thrust coefficient
C_Y	Linear approximation of lateral force coefficient
CS_o	Disturbance sensitivity transfer function
D_x	Reachability scaling matrix
dp, dq, dr	Angular velocity disturbances, rad/s
du, dv, dw	Translational velocity disturbances, m/s
F	Acceleration feed-forward matrix
g	Gravitational acceleration, m/s ²
G_d	Disturbance state space matrix
$H(s)$	Forming filter for Dryden turbulence velocities
I	Aircraft moment of inertia, kg m ²
$K_e(s)$	Equivalent controller transfer function for combined inner and outer loop

K_o	Outer loop control matrix
k_m	Motor coefficient for throttle
L	Dryden turbulence scale length, m
M	Acceleration feedback estimation matrix
m	Aircraft mass, kg
NS	Noise sensitivity transfer function
p, q, r	Roll, pitch, and yaw angular velocity, rad/s
Q, R	LQR controller weighting matrices
S	Aircraft wing area, m ²
S_{prop}, C_{prop}	Propeller disc area and coefficient
u, v, w	Forward, lateral, and heave translational velocity, m/s
V_a	Airspeed
x, y, z	Inertial position of the aircraft, m
X_c	Controllability gramian
X_d	Disturbance sensitivity gramian

Chapter 1

Introduction

1.1 Motivation

Small unmanned aircraft systems (sUAS) are being considered for many applications such as package delivery, search and rescue operations, crop monitoring, and military surveillance and reconnaissance. To perform these tasks, the aircraft must deal with environmental uncertainties including wind gusts and turbulence. In some cases like the storm-chasing aircraft in Figure 1.1, the vehicle is expected to fly stably through extreme winds. Fixed-wing sUAS are often controlled using successive feedback loops with a single input and a single output (SISO), which are unsuccessful in situations with strong gusts or damage to the aircraft that causes deviations from normal behavior [14]. The objective of this thesis is to develop an acceleration feedback control method for fixed-wing vehicles that enables more stable and controlled flight even in the presence of strong disturbances such as wind turbulence that are of the order of platform capabilities.

A sensor suite for fixed-wing sUAS generally includes GPS, an inertial measurement unit (IMU) with triaxial accelerometers, gyroscopes, and magnetometers, and static and dynamic pressure sensors [14], which provide measurements used to produce aircraft state estimates that are used in proportional-integral-derivative (PID), proportional-derivative (PD), or proportional-integral (PI) control [10, 35]. Fixed-wing control often involves PID loops using different dynamics assumptions and combinations of states estimated with the same set of sensors [27, 6, 7, 40]. Other methods involve complex nonlinear control schemes [9, 15, 33] that push the limits of autopilot systems that can be used on sUAS with limited payloads.



Figure 1.1: Fixed-wing aircraft such as this Twistor aircraft can be subjected to high winds while collecting weather data near a tornado.

More robust multi-input multi-output (MIMO) control methods have been successfully implemented for various types of aircraft, enabling stability and performance when facing model uncertainties and large disturbances. While MIMO control has been extensively explored with rotorcraft and other vehicles with high coupling between lateral and longitudinal dynamics [24, 23, 29], its implementation on fixed-wing vehicles has not been explored significantly. However, some research has explored robust H_∞ loop-shaping and μ -analysis-based methods for fixed-wing aircraft with improved disturbance rejection and uncertainty reduction [8, 25, 26, 29].

These MIMO control methods sometimes use a larger variety of sensors in order to estimate aircraft states. Distributed strain sensors and accelerometers have been proposed for force and moment estimation [22, 32] and force and moment feedback has been explored in simulated MIMO control, improving performance in the presence of uncertainties [37, 36]. Other studies skipped the force estimation and instead processed the sensor measurements using wide field integration or identified sensor models [11, 12].

Distributed inertial sensing has emerged from research examining biological flight, and provides improved redundancy and robustness. Insects use distributed mechanosensors to perform aerobatic, robust flight in the presence of disturbances [30]. Halteres are club-shaped flapping structures located behind a fly's wings (Figure 1.2). Different fly species show a large variation in haltere shape and sensilla placement (Figure 1.3) [5]. Despite this variation, all halteres measure

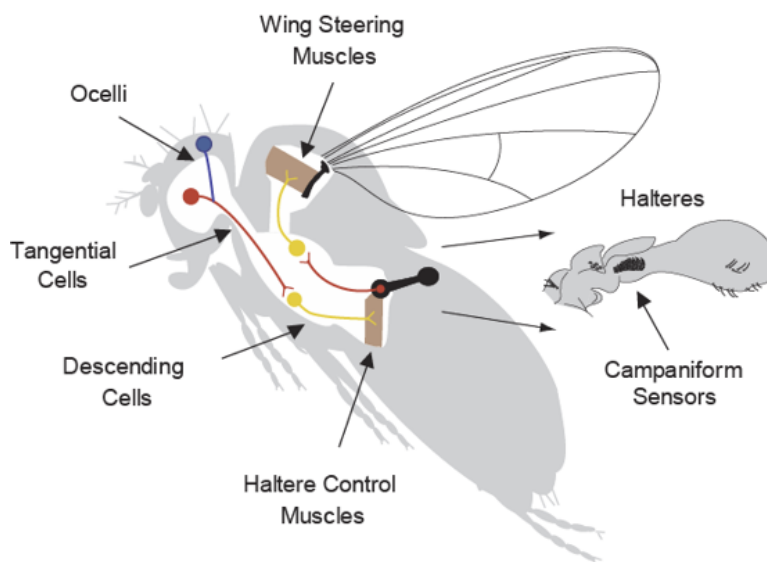


Figure 1.2: Basic outline of sensing, actuation, and control in a fly, including the halteres and campaniform sensilla which are used to measure forces and moments.

strain through distributed campaniform sensilla. Flies are able to measure forces and moments acting on their bodies by pooling the outputs of the sensilla. Flies cannot maintain stable flight when halteres are removed, suggesting that they are vital for robust and maneuverable flight [19]. Gyroscope and strain sensor design has been inspired by these biological sensors [39, 38].

Precise placement of a small number of accelerometers distributed from the center of gravity can be used to estimate translational and rotational acceleration states [16, 17]. These state estimates provide useful information about the forces and moments acting on the vehicle and can be used in feedback control for disturbance rejection [23]. The force-adaptive feedback method described in [23] motivated this research. The method was implemented by placing accelerometers on the quadrotor vehicle in Figure 1.4 to estimate translational and angular acceleration states. The states were estimated using linear least squares, with accelerometers were distributed away from the center of gravity in order to capture angular acceleration information. A system identification method was developed to determine the locations and orientations of the accelerometers as needed for state estimation. A nominal controller was augmented with an inner acceleration state feedback loop, including a feedforward term to prevent attenuation of desired accelerations.

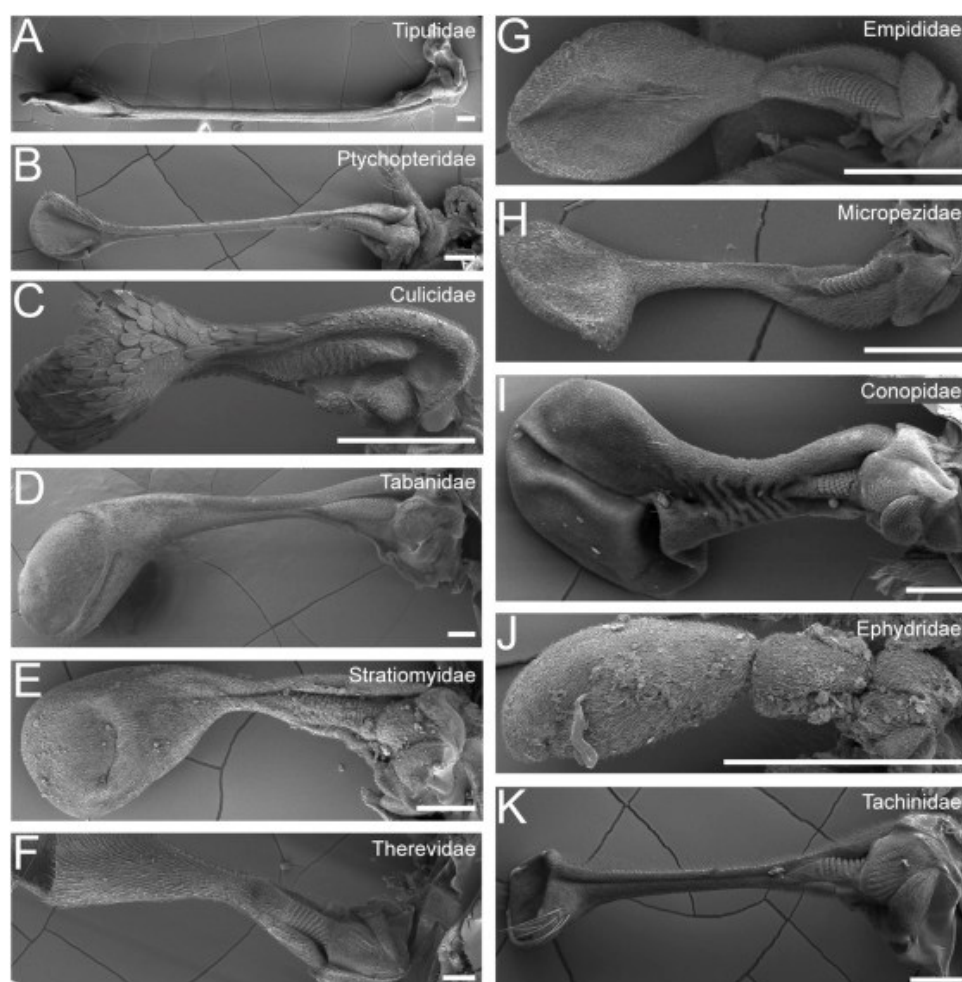


Figure 1.3: Scanning electron microscope images of a representative subset of fly halteres, showing large variations in shape (adapted from [5]).

The method provided improved disturbance rejection in 2 degree-of-freedom lateral motion of a quadrotor vehicle.

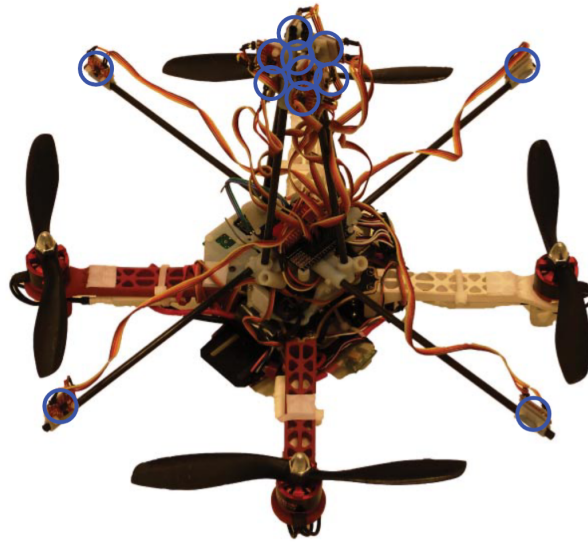


Figure 1.4: A quadrotor with distributed accelerometers (circled in blue) and force-adaptive feedback implementation (adapted from [23]).

1.2 Current Work

This work uses acceleration feedback to augment an existing fixed-wing autopilot for improved disturbance rejection. Acceleration states are fed back in an inner feedback loop which allows for quicker responses to disturbances such as wind gusts. The acceleration measurements essentially detect disturbing forces directly instead of sensing the position, pose, and velocity states after the disturbance propagates through the system. The main contribution of this work is the application of acceleration state feedback for a full 6-DOF fixed-wing UAS (instead of the 2-DOF, multirotor model in [23]) using nonlinear flight physics and demonstration of gust rejection. In practice the states would be estimated with distributed accelerometers, but for this work the acceleration states are assumed to be known.

The fixed-wing implementation introduces new challenges. Fixed-wing platforms tend to



Figure 1.5: CU Boulder's Ttwistor aircraft in flight.

be less maneuverable and more susceptible to gusts than multirotors [21]. Acceleration feedback has the potential to help fixed-wing platforms become more responsive and capable of rejecting disturbances even in turbulent environments. We will demonstrate this using a simulation of the Ttwistor aircraft (Figure 1.5), which has well-developed linear and nonlinear models.

1.3 Research Contributions

This research includes the following contributions to the field of fixed-wing unmanned aircraft systems control:

- (1) Synthesis and analysis of acceleration feedback control augmentation for fixed-wing aircraft in 6 degrees of freedom
 - (a) Identification of challenges for fixed-wing implementation of acceleration feedback
 - (b) Design of outer and inner loop controllers for a fixed-wing aircraft model
 - (c) Analysis of disturbance rejection performance improvement through closed-loop transfer function singular values and nonlinear simulation with wind turbulence
 - (d) Analysis of noise sensitivity of the closed-loop control method
- (2) Framework for gust sensitivity and maneuverability analysis of bare airframe fixed-wing dynamics to assess candidacy for acceleration feedback control

- (a) Analysis of disturbance sensitivity to quantify aircraft's open loop response to gusts
- (b) Analysis of maneuverability to characterize aircraft's potential for improved disturbance rejection by augmenting control

1.4 Organization

The thesis is organized as follows.

Chapter 2: In order to describe the simulation environment, the aircraft and environment models are outlined and discussed. This chapter details the nonlinear and linear aircraft models, and environmental wind model.

Chapter 3: Closed-loop aircraft disturbance rejection performance is limited by the capabilities of the aircraft itself. This chapter analyzes the open-loop aircraft model's maneuverability and disturbance sensitivity to determine whether it is a good candidate for acceleration feedback control.

Chapter 4: Controllers are often described by block diagrams. This chapter provides block diagrams and design methods for the outer loop (nominal) and inner loop (acceleration feedback) controllers used in this work, and the framework for distributed acceleration sensing.

Chapter 5: Controller performance for the acceleration feedback controller in comparison with the nominal controller can be analyzed via singular values, robust analysis, and simulated flight. This chapter gives the results of disturbance rejection, simulated wind gust tolerance, and noise rejection for the acceleration feedback controller in comparison with the nominal controller.

Chapter 6: This chapter provides a summary of the main results of the analysis of acceleration feedback control for fixed-wing vehicles, and suggests future work to support this research area.

Chapter 2

Model Structure

2.1 Overview

In this chapter, the simulation models for the aircraft and environment are described. The kinematics and dynamics of the Ttwistor aircraft used in this thesis were well-defined and tested by the Research and Engineering Center for Unmanned Vehicles (RECUV) team at the University of Colorado Boulder [31]. The force and moment equations (for lift, drag, and propulsive forces) were used to simulate a nonlinear model in Simulink (Figure 2.1). The actuators were also modeled to include saturation limits. The model was linearized about a straight-and-level flight trim condition to produce a linear state space model of the aircraft. This linear model was utilized for preliminary transfer function analysis as discussed in section 5.2. The simulation environment was set up to include Dryden turbulence to test disturbance rejection capabilities. In this chapter, the Dryden model will be described and turbulence parameters chosen.

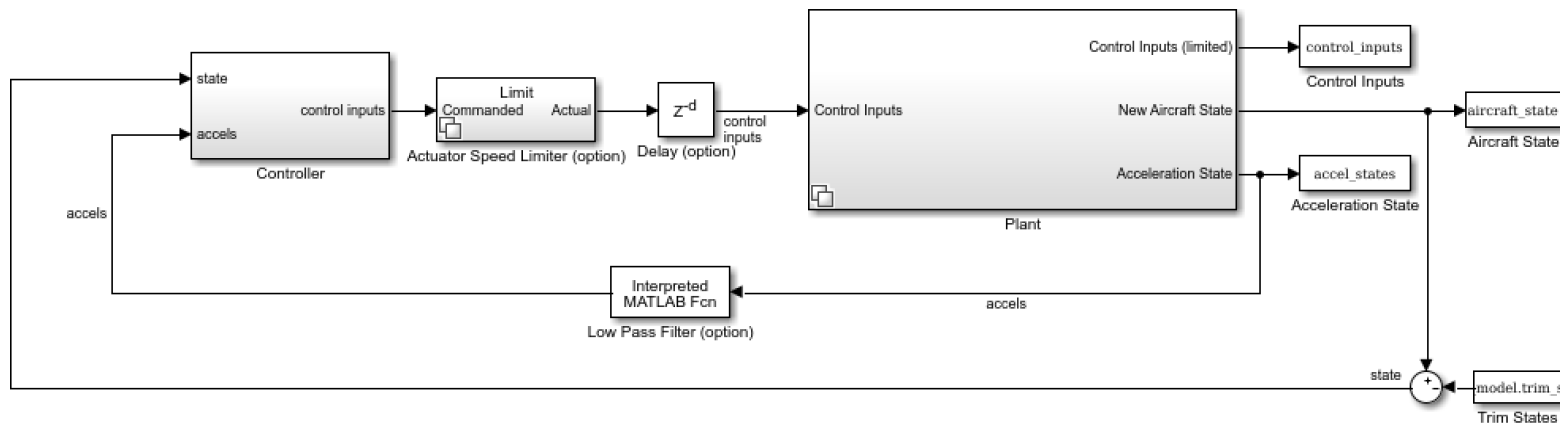


Figure 2.1: Simulink main block diagram for the nonlinear simulation.

2.2 Aircraft Model

The Ttwistor airframe (Figure 2.2) was chosen because both linear and nonlinear models were available [31]. The Ttwistor has twin engine-driven propellers to provide thrust, elevators and ailerons on the wings, and a rudder on its T-shaped tail. The configuration is common for fixed-wing vehicles. The geometric and mass properties of the Ttwistor aircraft are shown in Table 2.1.



Figure 2.2: Ttwistor aircraft being launched.

2.2.1 Nonlinear Model

A nonlinear model of the aircraft forces and moments was produced using the non-dimensional stability derivatives, engine and control surface parameters, moments of inertia, and aircraft geometry from [31]. For the nonlinear simulation, a Simulink model (Figure 2.4) was developed using the open loop nonlinear model outlined in Figure 2.3 and the controllers designed in Chapter 4. The aircraft's non-dimensional stability and control derivatives were used to calculate the forces and moments (\mathbf{F}_{net} and \mathbf{M}_{net}) acting on the aircraft considering the aircraft state \mathbf{x}_n , control inputs \mathbf{u}_n , surrounding wind disturbance \mathbf{d}_n , and air density ρ at the n^{th} timestep. The forces and moments were sent to the 6 degree of freedom equations of motion for a fixed-mass body to determine the

Table 2.1: Ttwistor aircraft geometry and mass properties.

Geometric				Mass			
Parameter	Symbol	Value	Units	Parameter	Symbol	Value	Units
Wing Span	b	3.067	m	Mass	m	5.74	kg
Wing Area	S	0.6282	m ²	Inertia	I_{xx}	1.2009	kg m ²
Mean Chord	c	0.208	m		I_{yy}	0.9318	kg m ²
					I_{zz}	2.0734	kg m ²
					I_{xz}	0.0946	kg m ²

new aircraft state and body-fixed acceleration. The individual blocks composing this model will be discussed in the next sections.

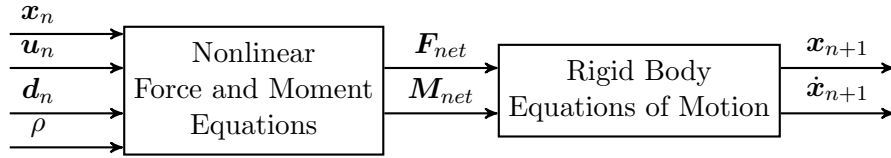


Figure 2.3: Open loop nonlinear model structure.

The aircraft state \mathbf{x} , control input \mathbf{u} , and disturbance \mathbf{d} vectors are defined:

$$\begin{aligned}
 \mathbf{x} &= \begin{bmatrix} x & y & z & \phi & \theta & \psi & u & v & w & p & q & r \end{bmatrix}^T \\
 \mathbf{u} &= \begin{bmatrix} \delta_e & \delta_a & \delta_r & \delta_t \end{bmatrix}^T \\
 \mathbf{d} &= \begin{bmatrix} du & dv & dw & dp & dq & dr \end{bmatrix}^T
 \end{aligned} \tag{2.1}$$

2.2.1.1 Kinematics and Dynamics

The 6 degree-of-freedom nonlinear equations of motion for the aircraft are solved using a pre-defined Simulink block for a rigid body with fixed mass. The right block in Figure 2.4 accepts as input the forces and moments acting on the body (in the body reference frame), and calculates the inertial position and velocity (in the inertial frame), Euler angles, direction-cosine matrix (DCM), and inertial and angular velocities and accelerations (in the body frame). The rigid body equations

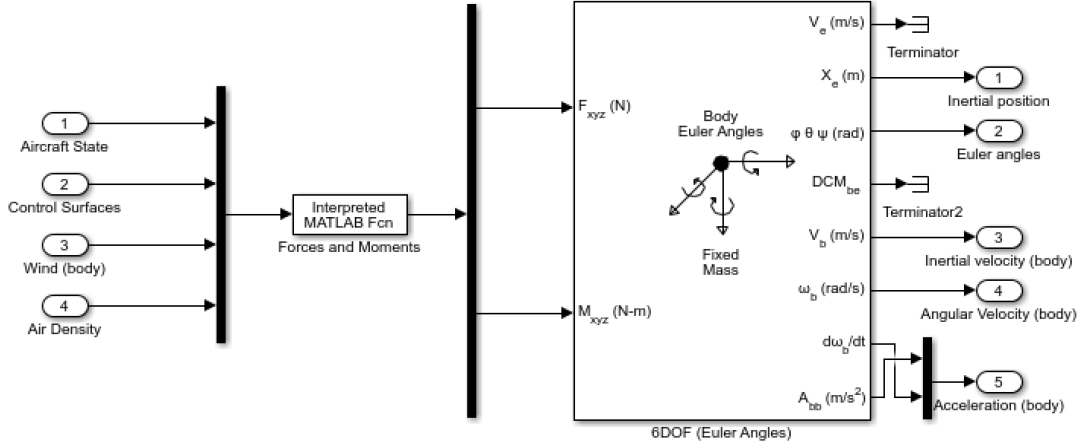


Figure 2.4: Simulink block diagram for the aircraft model subsystem, with force and moment calculations and 6 degree-of-freedom equations of motion.

of motion are well-defined and documented by MathWorks in [4]. The nonlinear aircraft simulation is further specified by the calculation of the aerodynamic forces and moments acting on the aircraft, as discussed in the next section (2.2.1.2).

2.2.1.2 Forces and Moments

The forces and moments acting on the aircraft are nonlinear with respect to aircraft states and control inputs, and can be separated into gravitational (\mathbf{F}_{grav}), propulsive (\mathbf{F}_{prop}), and aerodynamic forces and moments (\mathbf{F}_{aero} , \mathbf{M}_{aero}). Therefore, the net forces and moments acting on the aircraft are defined as follows:

$$\mathbf{F}_{net} = \mathbf{F}_{grav} + \mathbf{F}_{prop} + \mathbf{F}_{aero} \quad (2.2)$$

$$\mathbf{M}_{net} = \mathbf{M}_{aero}$$

The propulsive force will be described in the next section (2.2.1.3) detailing actuator models. Assuming the gravitational force acts at the center of mass of the vehicle, the weight produces only a force in the inertial z direction. Rotated into the aircraft body frame, this force relates to

the mass m and Euler angles of the vehicle (roll ϕ and pitch θ), and the gravitational acceleration constant g .

$$\mathbf{F}_{grav} = \begin{bmatrix} -mg \sin \theta \\ mg \cos \theta \sin \phi \\ mg \cos \theta \cos \phi \end{bmatrix} \quad (2.3)$$

The aerodynamic forces and moments are defined using the aircraft state, geometry parameters (b , c , S), nonlinear lift and drag models C_L and C_D , and linear approximations for pitching moment C_m as well as lateral forces and moments C_Y , C_l , and C_n .

$$\begin{aligned} \mathbf{F}_{aero} &= \begin{bmatrix} X \\ Y \\ Z \end{bmatrix} = \frac{1}{2} \rho V_a^2 S \begin{bmatrix} C_L \sin \alpha - C_D \cos \alpha \\ C_Y \\ -C_L \cos \alpha - C_D \sin \alpha \end{bmatrix} \\ \mathbf{M}_{aero} &= \begin{bmatrix} L \\ M \\ N \end{bmatrix} = \frac{1}{2} \rho V_a^2 S \begin{bmatrix} bC_l \\ cC_m \\ bC_n \end{bmatrix} \end{aligned} \quad (2.4)$$

The nonlinear lift and drag models are defined as:

$$\begin{aligned} C_L &= C_{L_0} + C_{L_\alpha} \alpha + C_{L_q} \frac{c}{2V_a} q + C_{L_{\delta_e}} \delta_e \\ C_D &= C_{D_{min}} + K(C_L - C_{L_{min}})^2 \end{aligned} \quad (2.5)$$

and the linear pitching moment and lateral forces and moments are modeled as:

$$\begin{aligned} C_m &= C_{m_0} + C_{m_\alpha} \alpha + C_{m_q} \frac{c}{2V_a} q + C_{m_{\delta_e}} \delta_e \\ C_Y &= C_{Y_0} + C_{Y_\beta} \beta + C_{Y_p} \frac{b}{2V_a} p + C_{Y_r} \frac{b}{2V_a} r + C_{Y_{\delta_a}} \delta_a + C_{Y_{\delta_r}} \delta_r \\ C_n &= C_{n_0} + C_{n_\beta} \beta + C_{n_p} \frac{b}{2V_a} p + C_{n_r} \frac{b}{2V_a} r + C_{n_{\delta_a}} \delta_a + C_{n_{\delta_r}} \delta_r \end{aligned} \quad (2.6)$$

In these equations, all double-subscripted coefficients C_{**} represent static and dynamic stability and control derivatives, determined using system identification and computational fluid dynamics (CFD) analysis of the Ttwistor [31].

2.2.1.3 Actuator Model

The control inputs were limited by upper and lower saturation values based on knowledge of fixed-wing control surfaces. The elevator, aileron and rudder were limited to $\pm\pi/2$ rad from their trim values, while the throttle was limited to range between 0 to 1 (given as a proportion of maximum thrust).

The propulsive force is calculated assuming the thrust vector is along the body x-axis, and there is negligible moment associated with the propeller. The propulsive force expressed in the body frame is defined:

$$\mathbf{F}_{prop} = \begin{bmatrix} \frac{1}{2}\rho V_a^2 S C_T \\ 0 \\ 0 \end{bmatrix} \quad (2.7)$$

where C_T is the thrust coefficient, defined using the propeller disc area S_{prop} and coefficient C_{prop} , motor constant k_m , throttle setting δ_t , aircraft geometry and airspeed as follows. Values are defined for the Ttwistor from system identification [31].

$$C_T = 2 \frac{S_{prop} C_{prop} \delta_t}{S V_a^2} [V_a + \delta_t (k_m - V_a)] [k_m - V_a] \quad (2.8)$$

2.2.1.4 Sensor Model

The simulations in Chapter 5 assume the aircraft's position and velocity states are known for outer loop control, but the acceleration states are estimated from sensors with noise for inner loop control. The outer loop controller was used as a baseline for comparison with the new control

method being analyzed requires a unique distributed sensing architecture with accelerometers and a gyroscope. These sensors were modeled to properly characterize the new controller’s performance. For this purpose, the sensor models used noise levels based on the Analog Devices ADXL325 accelerometer [1] and ADXRS450 gyroscope [2]. The noise was generated from a normal distribution with standard deviations of $0.025g$ and 0.13 deg/s for the accelerometer and gyroscope, respectively.

2.2.2 Linear Model

The goal of this section is to develop a linear model of the Ttwistor aircraft in state space form. In order to accomplish this, the nonlinear model must be linearized about a trim condition, as discussed in the next section.

2.2.2.1 Trim Condition

The aircraft parameters were used to produce a linear state space model for flight about a straight-and-level-flight trim condition. The condition was chosen for typical flight of the Ttwistor in Boulder, Colorado. The linear model assumes states and control inputs are modeled as perturbations from the trim condition. The trim states and control inputs are all zero except for those listed in Table 2.2.

Table 2.2: Ttwistor aircraft trim state and control inputs.

Trim State	Value	Units
h^*	1800	m
V_a^*	18	m/s
θ^*	0.0515	rad
u^*	17.9762	m/s
w^*	0.9263	m/s
Trim Input	Value	Units
δ_e^*	-0.537	rad
δ_t^*	17.92	% of max

2.2.2.2 State Space Model

The open loop aircraft system can be represented in state space form (Figure 2.5). The control inputs \mathbf{u} and external disturbance \mathbf{d} enter the plant, which in turn produces the states \mathbf{x} , state derivatives $\dot{\mathbf{x}}$, and outputs \mathbf{y} . The state space matrices A , B , C , and G_d are properties of the aircraft dynamics. The matrices utilize force and moment coefficients to characterize the aircraft. The coefficients were calculated using non-dimensional stability derivatives of the aircraft, which were determined by the system identification and CFD analysis in [31]. This reduced linear model was used for controller design and analysis. The aircraft model used 4 control inputs, 6 disturbance inputs, 8 states, and 4 outputs, separated into longitudinal and lateral directions:

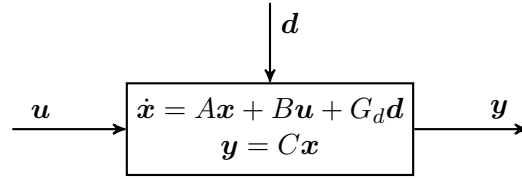


Figure 2.5: Open loop state space model.

$$\begin{aligned}
 \mathbf{u}_{lon} &= \begin{bmatrix} \delta_e & \delta_t \end{bmatrix}^T & \mathbf{u}_{lat} &= \begin{bmatrix} \delta_a & \delta_r \end{bmatrix}^T \\
 \mathbf{d}_{lon} &= \begin{bmatrix} du & dw & dq \end{bmatrix}^T & \mathbf{d}_{lat} &= \begin{bmatrix} dv & dp & dr \end{bmatrix}^T \\
 \mathbf{x}_{lon} &= \begin{bmatrix} u/V_a^* & w & q & \theta \end{bmatrix}^T & \mathbf{x}_{lat} &= \begin{bmatrix} v & p & r & \phi \end{bmatrix}^T \\
 \mathbf{y}_{lon} &= \begin{bmatrix} u/V_a^* & \theta \end{bmatrix}^T & \mathbf{y}_{lat} &= \begin{bmatrix} v & \phi \end{bmatrix}^T
 \end{aligned} \tag{2.9}$$

The longitudinal and lateral dynamics can be modeled by the following state space matrices, with

the force and moment coefficients for the Ttwistor defined in Table 2.3:

$$\begin{aligned}
 A_{lon} &= \begin{bmatrix} X_u & X_w/V_a^* & X_q/V_a^* & -g \cos \theta^*/V_a^* \\ Z_u V_a^* & Z_w & Z_q & -g \sin \theta^* \\ M_u V_a^* & M_w & M_q & 0 \\ 0 & 0 & 1 & 0 \end{bmatrix} & A_{lat} &= \begin{bmatrix} Y_v & Y_p & Y_r & g \cos \theta^* \\ L_v & L_p & L_r & 0 \\ N_v & N_p & N_r & 0 \\ 0 & 1 & \tan \theta^* & 0 \end{bmatrix} \\
 B_{lon} &= \begin{bmatrix} X_{\delta_e}/V_a^* & X_{\delta_t}/V_a^* \\ Z_{\delta_e} & 0 \\ M_{\delta_e} & 0 \\ 0 & 0 \end{bmatrix} & B_{lat} &= \begin{bmatrix} Y_{\delta_a} & Y_{\delta_r} \\ L_{\delta_a} & L_{\delta_r} \\ N_{\delta_a} & N_{\delta_r} \\ 0 & 0 \end{bmatrix} \\
 G_{d,lon} &= \begin{bmatrix} -X_u & -X_w/V_a^* & -X_q/V_a^* \\ -Z_u V_a^* & -Z_w & -Z_q \\ -M_u V_a^* & -M_w & -M_q \\ 0 & 0 & 0 \end{bmatrix} & G_{d,lat} &= \begin{bmatrix} -Y_v & -Y_p & -Y_r \\ -L_v & -L_p & -L_r \\ -N_v & -N_p & -N_r \\ 0 & 0 & 0 \end{bmatrix} \\
 C_{lon} &= \begin{bmatrix} 1 & 0 & 0 & 0 \\ 0 & 0 & 0 & 1 \end{bmatrix} & C_{lat} &= \begin{bmatrix} 1 & 0 & 0 & 0 \\ 0 & 0 & 0 & 1 \end{bmatrix}
 \end{aligned} \tag{2.10}$$

2.3 Disturbance/Environment Model

Wind was modeled using existing tools in Simulink, which include Dryden turbulence, discrete wind gusts, and wind shear models displayed in the block diagram (Figure 2.6) [4]. The wind translational and angular velocities (in the aircraft body frame) are provided by the Simulink blocks using the height, airspeed, and direction cosine matrix for the aircraft. The translational wind velocity vector \mathbf{V}_{wind} is subtracted from the aircraft velocity vector \mathbf{V}^E to produce the air relative velocity vector as $\mathbf{V}_B = \begin{bmatrix} u & v & w \end{bmatrix}^T = \mathbf{V}^E - \mathbf{V}_{wind}$. The air relative velocity vector is used

Table 2.3: Ttwistor aircraft linear model parameters.

Force Parameter	Value	Units	Moment Parameter	Value	Units
X_u	-0.1271	s^{-1}	L_v	-1.1467	$(m \cdot s)^{-1}$
X_w	0.6409	s^{-1}	L_p	-15.7093	s^{-1}
X_q	-0.9106	m/s	L_r	2.6774	s^{-1}
Y_v	-0.3714	s^{-1}	M_u	0.1090	$(m \cdot s)^{-1}$
Y_p	0.8254	m/s	M_w	-2.1148	$(m \cdot s)^{-1}$
Y_r	-17.6451	m/s	M_q	-3.2853	s^{-1}
Z_u	-0.7655	s^{-1}	N_v	0.6400	$(m \cdot s)^{-1}$
Z_w	-6.3237	s^{-1}	N_p	-1.2356	s^{-1}
Z_q	16.9091	m/s	N_r	-0.5669	s^{-1}
X_{δ_e}	0.0018	m/s^2	L_{δ_a}	-5.3580	s^{-2}
X_{δ_t}	3.3846	m/s^2	L_{δ_r}	0.0316	s^{-2}
Y_{δ_a}	-0.0137	m/s^2	M_{δ_e}	-1.3996	s^{-2}
Y_{δ_r}	0.0556	m/s^2	N_{δ_a}	-0.2566	s^{-2}
Z_{δ_e}	-0.1234	m/s^2	N_{δ_r}	-0.1309	s^{-2}

to calculate the airspeed V_a , angle of attack α , and sideslip β using the following expressions.

$$\begin{aligned} V_a &= \|\mathbf{V}_B\| \\ \alpha &= \arctan(w/u) \\ \beta &= \arcsin(v/V_a) \end{aligned} \quad (2.11)$$

The airspeed and wind angles are then used in the nonlinear force and moment calculations. The angular wind velocity vector $\boldsymbol{\omega}_{wind}$ provided by the Dryden turbulence model was added to the angular velocity of the aircraft as $\boldsymbol{\omega} = \boldsymbol{\omega}_B + \boldsymbol{\omega}_{wind}$.

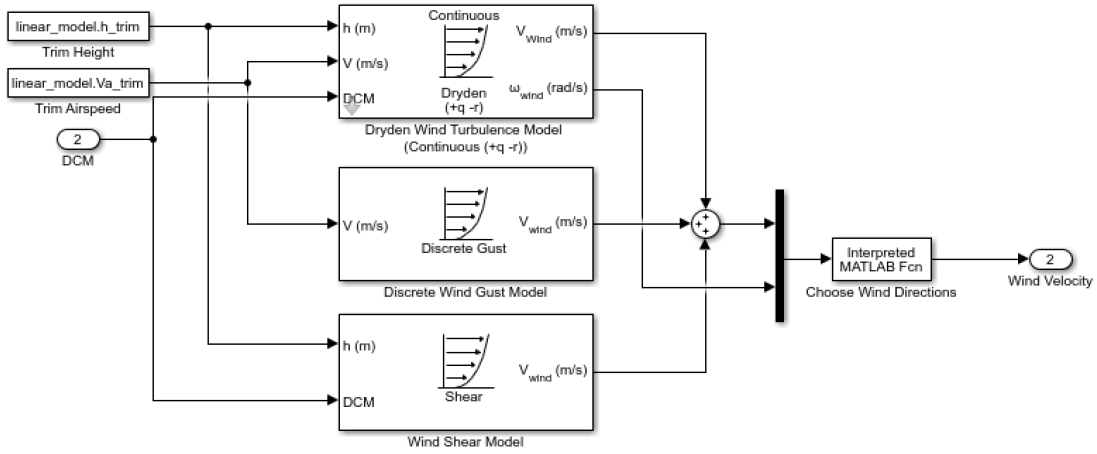


Figure 2.6: Simulink block diagram for modeling three types of wind, Dryden turbulence, discrete gusts, and wind shear.

2.3.0.1 Dryden Turbulence

The Dryden wind turbulence model was used to simulate wind for evaluation of the acceleration feedback control method. The turbulence was produced by passing band-limited white noise (with an upper limit of the simulation's time step) through a forming filter representing the relevant frequency content (Figure 2.7). The filtered white noise created simulated turbulence velocities in each of the 6 degrees of freedom of the system as $d = \begin{bmatrix} du & dv & dw & dp & dq & dr \end{bmatrix}^T$. The filters are

based on the power spectral densities of turbulence in each direction. The filters are described by the following transfer functions for each velocity direction (in aircraft body coordinates) as defined in [3]:

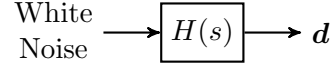


Figure 2.7: Model for Dryden wind turbulence with forming filters.

$$\begin{aligned}
 H_u(s) &= \sigma_u \sqrt{\frac{2L_u}{\pi V}} \frac{1}{1+(L_u/V)s} \\
 H_v(s) &= \sigma_v \sqrt{\frac{L_v}{\pi V}} \frac{1+(\sqrt{3}L_v/V)s}{(1+(L_v/V)s)^2} \\
 H_w(s) &= \sigma_w \sqrt{\frac{L_w}{\pi V}} \frac{1+(\sqrt{3}L_w/V)s}{(1+(L_w/V)s)^2}
 \end{aligned} \tag{2.12}$$

The wind magnitudes depend on the turbulence intensities $\sigma_{u,v,w}$ and scale lengths $L_{u,v,w}$ as well as the magnitude of the velocity of the aircraft V . The wind angular rates also depend on the aircraft's wingspan b and the other velocity intensities as

$$\begin{aligned}
 H_p(s) &= \sigma_w \sqrt{\frac{0.8}{V}} \frac{(\pi/4b)^{1/6}}{L_w^{1/3}(1+(4b/\pi V)s)} \\
 H_q(s) &= \frac{\pm s/V}{1+(4b/\pi V)s} H_w(s) \\
 H_r(s) &= \frac{\pm s/V}{1+(3b/\pi V)s} H_v(s)
 \end{aligned} \tag{2.13}$$

The turbulence intensities and scale lengths were chosen according to the vehicle's trim flight condition at 1800 m true altitude (above sea level), assuming moderate turbulence severity (with probability of exceedance 10^{-3}) as defined by [3]. For all wind velocity directions, $\sigma_{u,v,w} = 3.038\text{m/s}$ and $L_{u,v,w} = 533.4\text{m}$, and the aircraft's trim speed and wingspan of 18m/s and wingspan of 3.067m

were used as V and b , respectively. The magnitude of turbulence in each direction is described by the magnitude of each transfer function as a function of frequency with $s = j\omega$ (Figure 2.8).

The magnitudes of turbulence in the u , v , and w directions have a lower corner frequency in comparison to the angular rates. The angular rate magnitudes are low (less than 0.07 rad/s) for all frequencies. According to these plots, the wind disturbances of interest will be mainly in the velocity states u , v , w and will have frequencies of less than 1 rad/s. For frequencies greater than 1 rad/s, the largest turbulence magnitude is less than 0.6 m/s. The range of disturbance frequencies up to 1 rad/s (highlighted in Figure 2.8) will be considered when analyzing the disturbance rejection capabilities of the acceleration feedback controller in Chapter 5.

2.4 Conclusions

In this chapter, the simulation models for the aircraft and environment were described. The nonlinear force and moment equations for a small fixed-wing UAS were assembled with identified aerodynamic stability and control derivatives, and the model was linearized assuming small perturbations from a straight-and-level trim condition. The longitudinal and lateral linear models were decoupled to allow for separate analysis in the later performance section (Chapter 5). A simulation for applied wind disturbances was also outlined using the Dryden turbulence model. The turbulence parameters were chosen based on typical flight of the simulated Ttwistor aircraft at its trim condition. The shaping transfer functions for Dryden turbulence indicated that wind turbulence has significant magnitudes up to a frequency of 1 rad/s, so the controller should be able to reject disturbances up to this frequency.

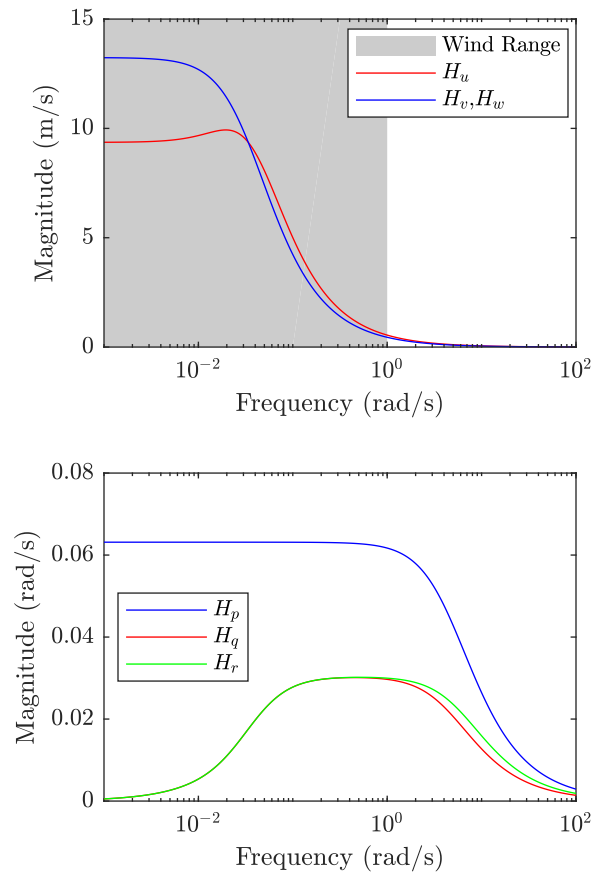


Figure 2.8: Dryden turbulence forming filter magnitudes for translational (top) and rotational (bottom) velocities.

Chapter 3

Assessment of Aircraft Candidacy for Augmented Control

3.1 Overview

The open loop aircraft model (in state space form) should be characterized before examining controller performance to ensure limitations are known. The aircraft's maneuverability can determine whether a more aggressive controller (such as acceleration feedback) may be unsuitable due to the platform's limitations. In addition, the aircraft's sensitivity to disturbances may determine whether an augmented controller is needed to maintain stability in the presence of disturbances. Both can be characterized using controllability gramians and disturbance sensitivity gramians, respectively, as outlined in [20]. This chapter will analyze the gramians of the Ttwistor aircraft to evaluate whether acceleration feedback control can be utilized to improve disturbance rejection performance, without closing the loop.

3.2 Maneuverability

Maneuverability is quantified by the set of reachable states in response to a bounded, unit-norm input ($\|u(t)\| \leq 1$). The reachable states represent the ellipsoid:

$$\varepsilon_c = \{X_c^{1/2}x_c : x_c \in \mathbb{R}^n \text{ and } \|u(t)\| \leq 1\} \quad (3.1)$$

with geometric properties defined by the infinite-time controllability gramian, using the aircraft

state space matrices from eqn (2.10):

$$X_c = \int_0^{\infty} e^{A\tau} BB' e^{A'\tau} d\tau \leq 0 \quad (3.2)$$

If the system is stable, the controllability gramian is calculated using the Lyapunov equation

$$AX_c + X_c A' + BB' = 0 \quad (3.3)$$

For an unstable but stabilizable system, the controllability gramian may be computed as shown in [41] using the Lyapunov equation

$$(A + BF)X_c + X_c(A + BF)' + BB' = 0 \quad (3.4)$$

with $F = -B'X$, where X is the stabilizing solution to the Riccati equation

$$XA + A'X - XBB'X = 0 \quad (3.5)$$

The resulting controllability gramian in either case provides the reachability ellipsoid's (ε_c) principal axis lengths and directions via the eigenvalues and eigenvectors of $X_c^{1/2}$, respectively. Longer ellipsoid axis lengths represent directions in which the aircraft is more maneuverable, as they require less energy to control. As in [20], the controllability gramian is normalized by a diagonal matrix based on expected maximum values of each state. For the Ttwistor aircraft, the longitudinal

and lateral scaling matrices are:

$$\begin{aligned}
 D_{x,lon} &= \begin{bmatrix} 1 & 0 & 0 & 0 \\ 0 & 5\text{m/s} & 0 & 0 \\ 0 & 0 & 10\text{rad/s} & 0 \\ 0 & 0 & 0 & 1.5\text{rad} \end{bmatrix} \\
 D_{x,lat} &= \begin{bmatrix} 5\text{m/s} & 0 & 0 & 0 \\ 0 & 10\text{rad/s} & 0 & 0 \\ 0 & 0 & 10\text{rad/s} & 0 \\ 0 & 0 & 0 & 1.5\text{rad} \end{bmatrix}
 \end{aligned} \tag{3.6}$$

to produce the normalized controllability gramians for each set of states as

$$\bar{X}_c = D_x^{-1} X_c D_x^{-1} \tag{3.7}$$

The size of the ellipsoid (and overall maneuverability of the vehicle in longitudinal and lateral directions) can then be quantified by the Frobenius norm of the controllability gramian:

$$\|\bar{X}_c^{1/2}\|_F = \sqrt{\text{trace}[(\bar{X}_c^{1/2})\bar{X}_c^{1/2}]} \tag{3.8}$$

The controllability gramians for the Ttwistor aircraft produce the ellipses in Figure 3.1 which are projected onto axes of each pair of states. The angular rate ellipses have longer axes in the roll rate p direction than the pitch or yaw rate (q or r) directions. This indicates that the aircraft's roll rate can be changed with less control effort than the pitch or yaw rates. For the velocity directions, the forward velocity u is already normalized by the trim airspeed to produce the state u/V_a^* . With a trim airspeed of 18 m/s, the ellipse axes are much larger in the forward velocity u direction than in lateral or upward velocities (v or w). The lateral velocity ellipse axis is slightly longer than the upward velocity axis, indicating that the aircraft can most easily change its forward velocity, and

Table 3.1: Frobenius norms of scaled maneuverability gramians for the Ttwistor and Skywalker.

$\ \bar{X}_c^{1/2}\ _F$	Longitudinal	Lateral	Overall
Ttwistor	0.6581	0.5983	0.8894
Skywalker	12.7291	15.5090	20.0639

has most difficulty changing its upward velocity. This is consistent with what we expect for a fixed-wing vehicle with typical control inputs. The engine directly changes forward acceleration, whereas the other control inputs (elevators, aileron, and rudder) affect the aircraft’s angular acceleration more directly than lateral or upward velocities. The maneuverability can be further characterized by the Frobenius norms of each of the scaled gramians (Table 3.1). The Frobenius norm is larger for longitudinal directions than lateral, so the aircraft is likely more maneuverable in its longitudinal states. This aircraft characteristic becomes a limitation later in Section 5.2, in which we analyze controller performance in both longitudinal and lateral directions. A more maneuverable aircraft will have increased benefits from inner-loop controllers (like the one in Chapter 4) because it will respond more quickly to fast control input changes. Thus, maneuverability is an important consideration for an aircraft’s candidacy for augmented control.

A smaller aircraft model’s maneuverability was quantified in comparison to the Ttwistor. Controllability gramians were calculated for the Skywalker 1880 (1.88m wingspan) linear state-space model from [13]. The model assumes a constant throttle setting to maintain the trim airspeed of 21.34 m/s, and therefore does not include longitudinal B matrix entries for throttle. The throttle simplification in this analysis may result in a lower maneuverability than you would see in reality for the Skywalker. The projected reachability ellipsoids for both the Skywalker and Ttwistor are presented in Figure 3.2, and the Frobenius norms are compared in Table 3.1. The Skywalker’s controllability ellipses are larger in all state directions and the Frobenius norms of the controllability gramians are over 20 times larger. This indicates that the Skywalker has a significant maneuverability advantage over the Ttwistor. Higher maneuverability should allow for faster disturbance rejection with the more aggressive inner loop controllers described in Chapter 4.

3.3 Disturbance Sensitivity

Similarly to the maneuverability analysis, the disturbance sensitivity of the aircraft may be analyzed to quantify the need for augmented control. The set of reachable states for the system in response to a bounded disturbance input $\|d\| \leq 1$ are equivalent to the ellipsoid

$$\varepsilon_d = \{X_d^{1/2}x_d : x_d \in \mathbb{R}^n \text{ and } \|d(t)\| \leq 1\} \quad (3.9)$$

Where the disturbance sensitivity gramian is computed using the aircraft state space matrices A and G_d in the Lyapunov equation:

$$AX_d + X_dA' + G_dG_d' = 0 \quad (3.10)$$

for a stable system. For an unstable but stabilizable system, the disturbance sensitivity gramian is

$$X_d = \frac{1}{2\pi} \int_{-\infty}^{\infty} (j\omega I - A)^{-1} G_d G_d' (-j\omega I - A')^{-1} d\omega \quad (3.11)$$

with the solution from the Lyapunov equation

$$(A + G_d F)X_d + X_d(A + G_d F)' + G_d G_d' = 0 \quad (3.12)$$

where $F = -G_d'X$, where X is the stabilizing solution to the Riccati equation

$$XA + A'X - XG_dG_d'X = 0 \quad (3.13)$$

The resulting disturbance sensitivity gramian provides the lengths and directions of the disturbance sensitivity ellipsoid axes through the eigenvalues and eigenvectors of $X_d^{1/2}$. Longer axes represent that the aircraft may be pushed in that direction with less disturbance energy. Again, the gramian

Table 3.2: Frobenius norms of scaled disturbance sensitivity gramians for the Ttwistor and Skywalker.

$\ \bar{X}_d^{1/2}\ _F$	Longitudinal	Lateral	Overall
Ttwistor	3.2009	2.9853	4.3770
Skywalker	6.0726	2.4780	6.5587

is normalized using diagonal scaling matrices and the Frobenius norm is computed to quantify the aircraft's overall disturbance sensitivity in longitudinal and lateral directions.

The disturbance sensitivity ellipses for the Ttwistor and Skywalker aircraft are represented in Figure 3.3. The longer ellipse axes indicate that the aircraft is more susceptible to disturbances in those directions. The Ttwistor is nearly equally sensitive to disturbances in all angular rate and Euler angle states. For velocity states, remembering that the forward velocity state is normalized, the Ttwistor is most sensitive to forward velocity disturbances and least sensitive to heave velocity disturbances. The Frobenius norms of the scaled sensitivity gramians (Table 3.2) further indicate that both aircraft are more susceptible to longitudinal disturbances than lateral, as the norms are larger for the longitudinal gramians. Augmented control may be more useful in longitudinal directions for these aircraft because of their increased sensitivity. The overall sensitivities of the two aircraft are characterized by the Frobenius norms of the full gramians with longitudinal and lateral components. The Skywalker is marginally more sensitive to wind gusts and may benefit more from an augmented controller for disturbance rejection.

3.4 Conclusions

The aircraft characteristics affecting the success of augmented control have been discussed. A platform's maneuverability affects whether more aggressive control signals will propagate into aircraft states fast enough to provide improvement in disturbance rejection. Sensitivity has also been quantified to determine whether an aircraft is affected by external disturbances enough to necessitate augmented control. Two aircraft models were compared using both of these analyses. Aircraft with high maneuverability and high sensitivity (as characterized by the controllability

and sensitivity gramians) make good candidates for the control scheme described in Chapter 4 for significant disturbance rejection improvement.

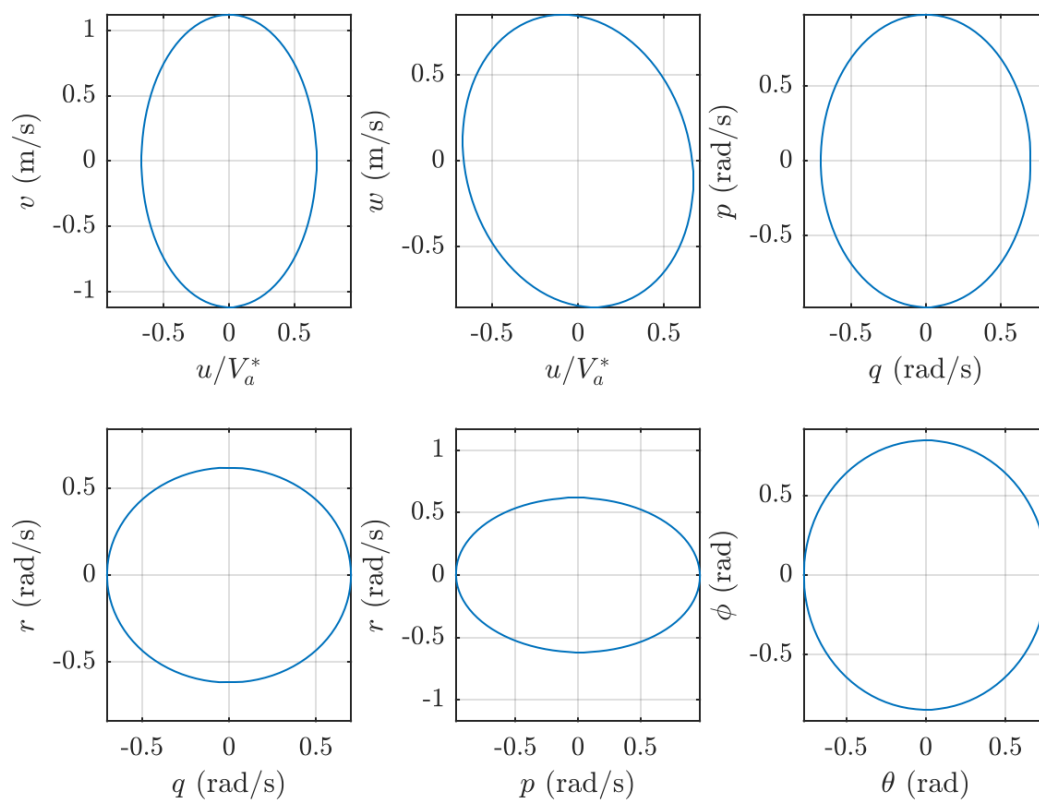


Figure 3.1: Maneuverability ellipses for the Ttwistor open loop aircraft model.

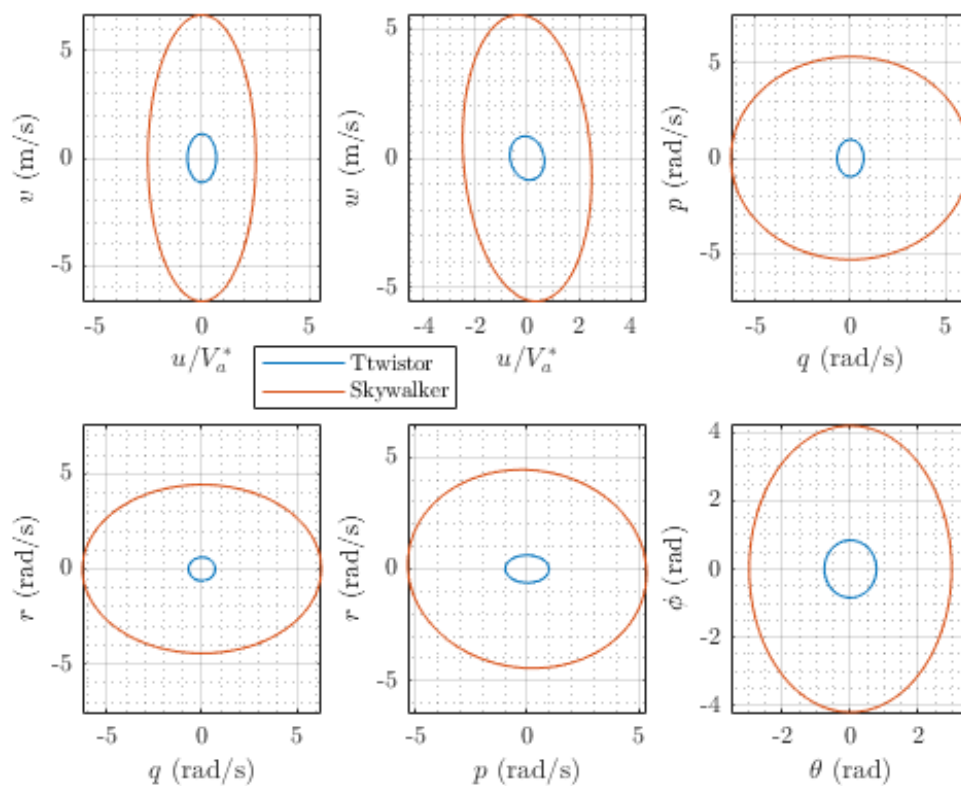


Figure 3.2: Comparison of maneuverability ellipses for the Twistor and Skywalker open loop aircraft models.

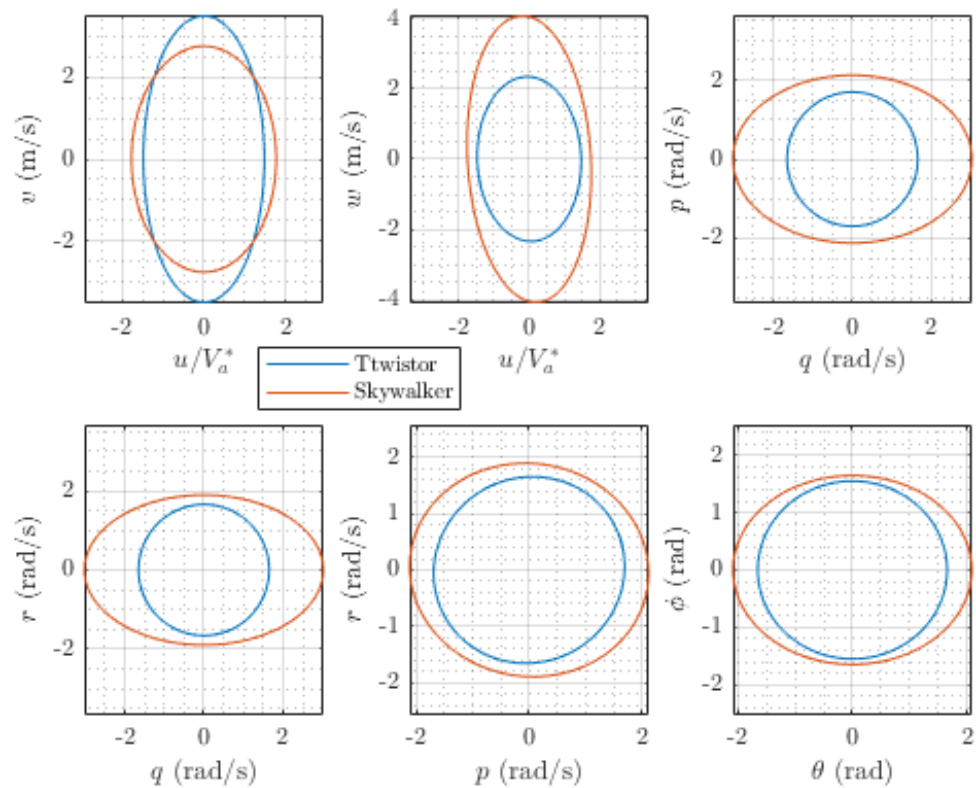


Figure 3.3: Comparison of disturbance sensitivity ellipses for the Twistor and Skywalker open loop aircraft models.

Chapter 4

Control Design

4.1 Overview

The acceleration feedback control scheme is described in this chapter. A nominal outer loop controller is chosen as a baseline for comparison. The outer loop controller is augmented with acceleration feedback and feedforward terms to improve disturbance rejection performance. Acceleration feedback allows for faster responses to external disturbances because the inner loop feeds back acceleration states, instead of adjusting control inputs after the disturbance propagates through velocity and position states. The block diagrams for the nominal and acceleration feedback control methods are outlined in the following sections. The acceleration state estimation method through distributed acceleration sensing is explained in section 4.4.

4.2 Outer Loop Controller

There are several types of MIMO controllers; for this work a linear-quadratic-regulator (LQR) controller was chosen for the outer loop. The LQR method uses weighting matrices representing the desired performance and control bounds to calculate an optimal stabilizing controller K_o , a matrix which forces the states \mathbf{x} to zero while satisfying actuator limits. The nominal feedback control system is shown in Figure 4.1 with the plant in state space form and the LQR controller acting on the states.

For the Ttwistor aircraft, the Q and R weighting matrices were chosen to maximize attenuation of the output states while limiting the control inputs enough to avoid saturation. The LQR

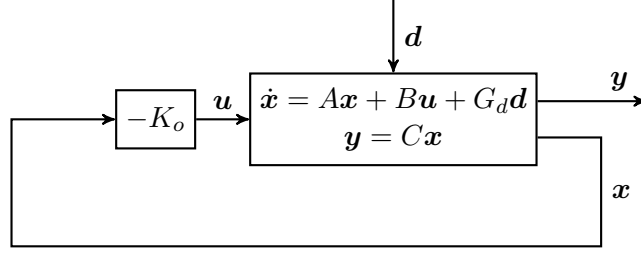


Figure 4.1: Nominal LQR control model.

controllers were designed separately for longitudinal and lateral directions, then combined into a single matrix. The Q and R matrices were defined:

$$\begin{aligned}
 Q_{lon} &= \begin{bmatrix} 50 & 0 & 0 & 0 \\ 0 & 0 & 0 & 0 \\ 0 & 0 & 0 & 0 \\ 0 & 0 & 0 & 50 \end{bmatrix} & Q_{lat} &= \begin{bmatrix} 1 & 0 & 0 & 0 \\ 0 & 0 & 0 & 0 \\ 0 & 0 & 0 & 0 \\ 0 & 0 & 0 & 1 \end{bmatrix} \\
 R_{lon} &= \begin{bmatrix} 5 & 0 \\ 0 & 10 \end{bmatrix} & R_{lat} &= \begin{bmatrix} 5 & 0 \\ 0 & 50 \end{bmatrix}
 \end{aligned} \tag{4.1}$$

These weighting matrices produced the following outer loop LQR controllers for longitudinal and lateral directions:

$$\begin{aligned}
 K_{o,lon} &= \begin{bmatrix} -0.4413 & 0.1025 & -0.3348 & -2.9343 \\ 1.9260 & -0.0053 & 0.0303 & 0.1724 \end{bmatrix} \\
 K_{o,lat} &= \begin{bmatrix} -0.0047 & -0.1136 & 0.5472 & -1.0983 \\ 0.0018 & 0.0026 & -0.0248 & 0.0117 \end{bmatrix}
 \end{aligned} \tag{4.2}$$

The outer loop LQR controller was augmented with inner loop acceleration feedback as discussed in the next section.

4.3 Inner Loop Acceleration Feedback

In this work, the nominal LQR controller was augmented with an inner loop for acceleration state feedback as described in [23] (Figure 4.2). The translational and rotational acceleration states $\mathbf{x}_a = \begin{bmatrix} \dot{u} & \dot{v} & \dot{w} & \dot{p} & \dot{q} & \dot{r} \end{bmatrix}^T$ were chosen with the feedback estimation matrix M . Simply feeding back the total acceleration on the aircraft will attenuate gust disturbances, but will additionally suppress desired vehicle accelerations caused by pilot command inputs, which need to be compensated for using a feed-forward term. The specific form of the feed-forward term has been shown to be $F = MB$ in [23]. The feed-forward matrix mapped the outer loop controller's actuator commands \mathbf{u}_o into desired acceleration states, which were subtracted from the total acceleration states, leaving only the accelerations due to disturbances, and fed to the inner loop control matrix K_i . The inner loop matrix to map accelerations to control inputs was defined as the pseudoinverse of F , or

$$K_i = ((MB)^T MB)^{-1} (MB)^T \quad (4.3)$$

For the longitudinal and lateral directions, the following matrices resulted:

$$K_{i,lon} = \begin{bmatrix} 0 & -0.0625 & -0.7090 \\ 5.3182 & 0 & 0.0004 \end{bmatrix} \quad (4.4)$$

$$K_{i,lat} = \begin{bmatrix} 0.0123 & -0.1848 & -0.0394 \\ 0.2701 & 0.0300 & -0.6420 \end{bmatrix}$$

This controller produced augmented control inputs \mathbf{u} which were modified based on the accelerations of the vehicle. For the nonlinear simulation in this paper, the inner loop control matrix K_i was adjusted by placing a reduced 1/10 weight on the row corresponding to the rudder control input δ_r . The above definition of K_i caused saturation and chopping of the rudder in initial simulations, so the weighting was manually reduced. This produced more reasonable rudder

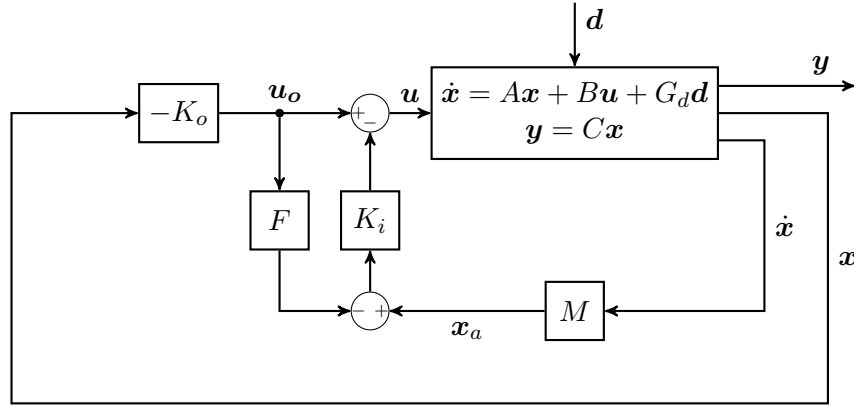


Figure 4.2: Augmented control with acceleration feedback.

commands as discussed in Chapter 5.

Disturbances immediately and directly impact the acceleration states of the aircraft, allowing the autopilot with acceleration feedback to respond more quickly. Disturbance rejection was verified through controller analysis and nonlinear simulations, as discussed in Chapter 5.

In the nonlinear simulation, the acceleration states were calculated from the equations of motion of the aircraft. Numerical differentiation performed in MATLAB created high frequency noise in the acceleration states at the simulation's time step. To resolve this, the acceleration states were processed with a low-pass weighted average filter with equation

$$\dot{\mathbf{x}}_{LPF,n} = 0.9\dot{\mathbf{x}}_{LPF,(n-1)} + 0.1\dot{\mathbf{x}}_n \quad (4.5)$$

where $\dot{\mathbf{x}}_{LPF,n}$ is the low-pass-filtered acceleration state vector at the current time step, and is calculated using the previous low pass filtered accelerations and the current acceleration state vector.

4.4 Distributed Acceleration Sensing

The acceleration state vector of the aircraft will be used in the next section for acceleration feedback control. A collection of tri-axial accelerometers are distributed across the fuselage to esti-

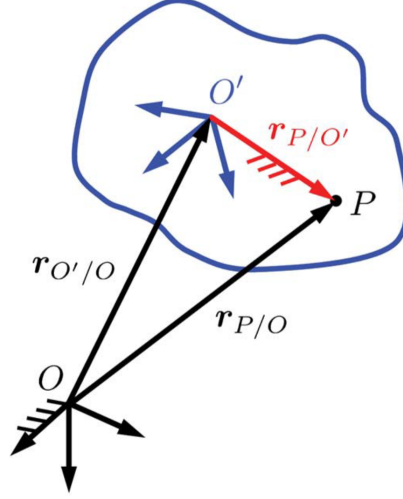


Figure 4.3: Coordinate frames for the acceleration of a point P on the rigid body O' with respect to the inertial frame O (reproduced from [23]).

mate the translational and rotational accelerations of the vehicle, given in the inertial acceleration state vector:

$$\mathbf{x}_a^E = \begin{bmatrix} a_x & a_y & a_z & \dot{p} & \dot{q} & \dot{r} & p^2 & q^2 & r^2 & pq & pr & qr \end{bmatrix}^T \quad (4.6)$$

The state estimation is performed using a modified version of the method outlined in [23]. The inertial acceleration with respect to the inertial frame O at the point P of any accelerometer placed away from the vehicle center of mass O' (Figure 4.3) is given by:

$$\mathbf{a}_{P/O} = \mathbf{a}_{O'/O} + \mathbf{a}_{P/O'} + \boldsymbol{\alpha} \times \mathbf{r}_{P/O'} + 2\boldsymbol{\omega} \times \mathbf{v}_{P/O'} + \boldsymbol{\omega} \times (\boldsymbol{\omega} \times \mathbf{r}_{P/O'}) \quad (4.7)$$

with the following definitions:

- (1) $\mathbf{a}_{O'/O}$ is the translational acceleration of the vehicle center of mass with respect to the inertial frame
- (2) $\mathbf{a}_{P/O'}$ is the translational acceleration of P with respect to O'

(3) $\mathbf{r}_{P/O'}$ is the position vector of point P with respect to the center of mass O'

(4) $\boldsymbol{\alpha} \times \mathbf{r}_{P/O'}$ is the Euler acceleration of the vehicle

(5) $2\boldsymbol{\omega} \times \mathbf{v}_{P/O'}$ is the Coriolis acceleration of the vehicle

(6) $\boldsymbol{\omega} \times (\boldsymbol{\omega} \times \mathbf{r}_{P/O'})$ is the centripetal acceleration of the vehicle

Given the assumption that the aircraft fuselage is a rigid body, the position vector $\mathbf{r}_{P/O'}$ is constant in the body-fixed frame and its derivatives ($\mathbf{v}_{P/O'}$ and $\mathbf{a}_{P/O'}$) are zero. Terms (2) and (5) are now removed from the equation to produce the following for the acceleration at each accelerometer location:

$$\mathbf{a}_{P/O} = \mathbf{a}_{O'/O} + \boldsymbol{\alpha} \times \mathbf{r}_{P/O'} + \boldsymbol{\omega} \times (\boldsymbol{\omega} \times \mathbf{r}_{P/O'}) \quad (4.8)$$

This is a linear relationship which can be used to relate the total acceleration \mathbf{a}_i at the i th accelerometer located at position $\mathbf{r}_i = \begin{bmatrix} r_{x,i} & r_{y,i} & r_{z,i} \end{bmatrix}^T$ to the inertial acceleration state vector of the vehicle \mathbf{x}_a^E as

$$\mathbf{a}_i = \begin{bmatrix} 1 & 0 & 0 & 0 & r_{z,i} & -r_{y,i} & 0 & -r_{x,i} & -r_{x,i} & r_{y,i} & r_{z,i} & 0 \\ 0 & 1 & 0 & -r_{z,i} & 0 & r_{x,i} & -r_{y,i} & 0 & -r_{y,i} & r_{x,i} & 0 & r_{z,i} \\ 0 & 0 & 1 & r_{y,i} & -r_{x,i} & 0 & -r_{z,i} & -r_{z,i} & 0 & 0 & r_{x,i} & r_{y,i} \end{bmatrix} \mathbf{x}_a^E \quad (4.9)$$

When combined with sensor characteristics, this is used to represent each uniaxial accelerometer measurement z_i of the total acceleration \mathbf{a}_i using the position \mathbf{r}_i , orientation $\hat{\mathbf{e}}_i$, scale factor κ_i and bias b_i of the i th accelerometer:

$$z_i = \kappa_i \hat{\mathbf{e}}_i^T \mathbf{a}_i + b_i \equiv \mathbf{c}_i^T \mathbf{x}_a^E + b_i \quad (4.10)$$

where the orientation unit vector is expressed using the azimuth and elevation angles (γ_i, β_i) with

respect to the body x axis as

$$\hat{\mathbf{e}}_i \equiv \begin{bmatrix} \cos \gamma_i \cos \beta_i & \sin \gamma_i \cos \beta_i & -\sin \beta_i \end{bmatrix}^T \quad (4.11)$$

The sensor characteristic constants $(\kappa_i, b_i, \gamma_i, \beta_i, r_{x,i}, r_{y,i}, r_{z,i})$ fully define the relationship between \mathbf{x}_a^E and z_i . The n sensor measurements and characteristic matrices are concatenated to produce an accelerometer measurement vector \mathbf{z} as

$$\mathbf{z} \equiv \begin{bmatrix} z_1 \\ z_2 \\ \vdots \\ z_n \end{bmatrix} = \begin{bmatrix} \mathbf{c}_1^T \\ \mathbf{c}_2^T \\ \vdots \\ \mathbf{c}_n^T \end{bmatrix} \mathbf{x}_a + \begin{bmatrix} b_1 \\ b_2 \\ \vdots \\ b_n \end{bmatrix} \equiv C_a \mathbf{x}_a + \mathbf{b} \quad (4.12)$$

where the matrix $C_a = C_a(\mathbf{r}, \kappa, \gamma, \beta)$ has dimension $n \times 12$. The relationship is inverted to produce the acceleration state vector estimate using the pseudoinverse C_a^\dagger as

$$\hat{\mathbf{x}}_a^E = (C_a^T C_a)^{-1} C_a^T (\mathbf{z} - \mathbf{b}) \equiv C_a^\dagger (\mathbf{z} - \mathbf{b}) \quad (4.13)$$

Assuming the sensors have additive, zero-mean Gaussian noise, this equation represents the optimal linear estimator [18, 28].

With small-perturbation assumptions for the rotational rates based on straight and level flight (i.e. $\Delta p \Delta q \approx \Delta p \Delta r \approx \Delta q \Delta r \approx \Delta p^2 \approx \dots \approx 0$), the estimated acceleration state condenses to

$$\hat{\mathbf{x}}_a^E = \begin{bmatrix} \hat{a}_x & \hat{a}_y & \hat{a}_z & \hat{p} & \hat{q} & \hat{r} \end{bmatrix} \quad (4.14)$$

The additional assumption of a quadrotor in hover in [23] allowed for the acceleration states to be equated as $\hat{a}_x \approx \hat{u}$, $\hat{a}_y \approx \hat{v}$, and $\hat{a}_z \approx \hat{w}$. This does not apply for a fixed-wing vehicle in forward

flight, which always has nonzero forward velocity. Therefore, we must also apply the equations:

$$\begin{aligned}
 a_x &= \dot{u} + qw - rv \\
 a_y &= \dot{v} + ru - pw \\
 a_z &= \dot{w} + pv - qu
 \end{aligned} \tag{4.15}$$

These equations can be rearranged to describe the desired states $(\hat{u}, \hat{v}, \hat{w})$ and linearized about the straight-and-level flight trim condition for fixed-wing aircraft to produce the following:

$$\begin{aligned}
 \hat{u} &= \hat{a}_x - \hat{q}w^* \\
 \hat{v} &= \hat{a}_y - \hat{r}u^* + \hat{p}w^* \\
 \hat{w} &= \hat{a}_z + \hat{q}u^*
 \end{aligned} \tag{4.16}$$

where the rotational velocities $(\hat{p}, \hat{q}, \hat{r})$ are directly measured and estimated using a triaxial gyroscope on the vehicle. The lateral velocity is assumed to be small ($\Delta v \approx 0$), and the forward and heave velocities are approximated based on the straight-and-level flight trim condition ($u \approx u^*$ and $w \approx w^*$). The velocities are approximated by the trim conditions because of the lack of sensors available to directly measure these states on a general fixed-wing vehicle. The velocity states could also be estimated with a Kalman filter on GPS, IMU, or pitot tube data; this process is omitted in this work for simplicity. Therefore, distributed accelerometers and a triaxial gyroscope can be used with the equations above for estimating the acceleration state vector to produce:

$$\hat{\mathbf{x}}_a = \begin{bmatrix} \hat{u} & \hat{v} & \hat{w} & \hat{p} & \hat{q} & \hat{r} \end{bmatrix}^T \tag{4.17}$$

Analysis of the accelerometer estimation scheme with different numbers and positions of sensors is available in [23]. At least 8 uniaxial sensors need to be placed in non-coplanar locations to produce a non-singular estimation matrix (C_a). Placing accelerometers further away from the center of gravity of the vehicle has been shown to reduce estimation error. It is not recommended to

place accelerometers on the wings, as the rigid body equations would no longer be valid considering the wings' flexibility. For the nonlinear simulations in this work, 4 triaxial accelerometers (12 uniaxial) were simulated with positions on the surface of a 10cm-radius sphere centered around the center of gravity of the aircraft (Figure 4.4), with the sensing axes aligned with the aircraft body axes. This is a conservative placement for the Ttwistor aircraft, which could have sensors placed farther away from the center of gravity along the full fuselage length.

4.5 Conclusions

The acceleration feedback control method has been outlined in this chapter. A full-state-feedback LQR controller was designed for the outer loop, and acceleration feedback and feedforward matrices for the inner loop. The LQR controller alone will be used as a baseline for performance comparison in Chapter 5. The augmented control method with acceleration feedback should provide quicker and more robust disturbance rejection by adjusting control inputs based on acceleration states rather than lower-order velocity and position states. The acceleration state estimation equations have also been described and adjusted for fixed-wing implementation.

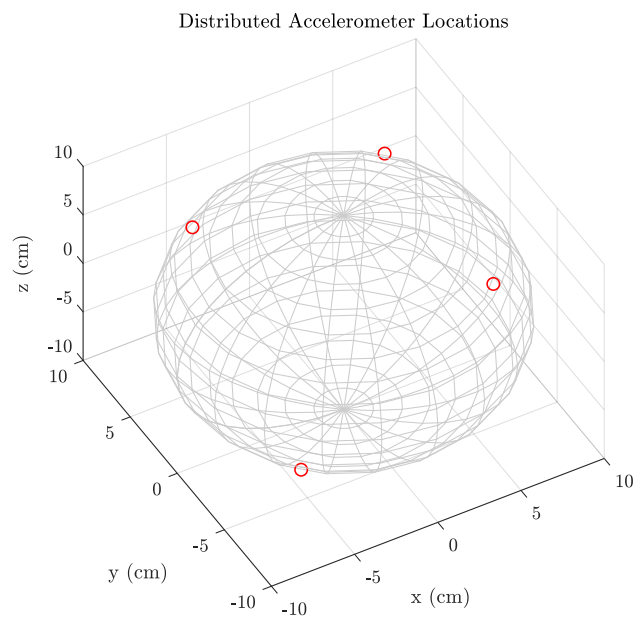


Figure 4.4: Modeled locations of the 4 triaxial accelerometers used for simulation, which are on the surface of a 10cm-radius sphere.

Chapter 5

Performance Analysis

5.1 Overview

The performance of the nominal and acceleration feedback controllers can be compared through various methods. Disturbance rejection and sensitivity to accelerometer noise can be characterized over frequency through sensitivity transfer functions. In addition, nonlinear flight simulations with Dryden turbulence are used to compare gust rejection performance.

5.2 Disturbance Rejection

The improvement in disturbance rejection was analyzed through the frequency response of the closed loop transfer function matrices for both nominal and acceleration feedback control. The acceleration feedback controller was collapsed into an equivalent transfer function matrix by following the path from states \mathbf{x} to control inputs \mathbf{u} . The state derivatives $\dot{\mathbf{x}}$ are equivalent to the transfer function $s\mathbf{x}$, and the outer loop controller's commands \mathbf{u}_o are calculated using $\mathbf{u}_o = -K_o\mathbf{x}$.

$$\begin{aligned}\mathbf{u} &= \mathbf{u}_o - K_i(M\dot{\mathbf{x}} - F\mathbf{u}_o) \\ &= -K_o\mathbf{x} - K_i(M\dot{\mathbf{x}} + FK_o\mathbf{x}) \\ &= -K_o\mathbf{x} - K_i(Ms\mathbf{x} + FK_o\mathbf{x}) \\ &= -(K_o + K_iMs + K_iFK_o)\mathbf{x}\end{aligned}\tag{5.1}$$

This produces the equivalent controller transfer function for the controller with inner accel-

eration feedback:

$$K_e(s) = K_o + K_i M s + K_i F K_o \quad (5.2)$$

The equivalent controller was used to calculate the closed loop transfer functions. The transfer function to map the disturbance \mathbf{d} (as illustrated in the block diagrams in Figures 2.5-4.2) to the states \mathbf{x} was calculated as

$$\begin{aligned} \dot{\mathbf{x}} &= A\mathbf{x} + B\mathbf{u} + G_d\mathbf{d} \\ &= A\mathbf{x} - BK\mathbf{x} + G_d\mathbf{d} \\ \mathbf{x} &= (sI - A + BK)^{-1}G_d\mathbf{d} \end{aligned} \quad (5.3)$$

Where K can be substituted to represent either the nominal controller (K_o) or augmented acceleration feedback controller (K_e). Continuing to the plant outputs \mathbf{y} produces

$$\begin{aligned} \mathbf{y} &= C\mathbf{x} \\ \mathbf{y} &= C(sI - A + BK)^{-1}G_d\mathbf{d} \end{aligned} \quad (5.4)$$

This provides the sensitivity transfer function matrix CS_o which maps the disturbance \mathbf{d} to the plant output \mathbf{y} as

$$CS_o = C(sI - A + BK)^{-1}G_d \quad (5.5)$$

The frequency response of this transfer function matrix was analyzed by calculating the maximum singular values $\bar{\sigma}(CS_o)$ as is common for robust analysis [34]. The maximum singular values for CS_o represent the largest transfer of disturbance energy to output energy. Lower singular values indicate better disturbance rejection, as less energy is allowed to propagate from the disturbance to the output. Figure 5.1 shows the sensitivity singular values for both nominal and acceleration

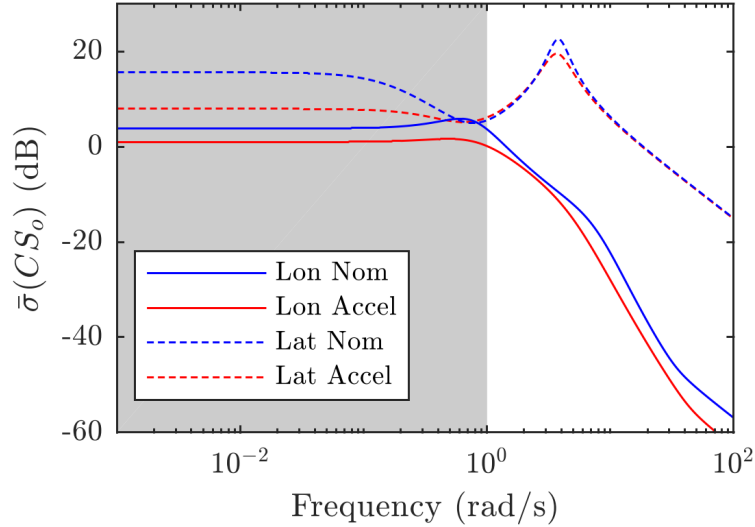


Figure 5.1: Sensitivity singular values for both controllers, in lateral (top) and longitudinal (bottom) directions.

feedback controllers; the top two curves are for lateral directions, and the bottom two are for longitudinal. The shaded region represents disturbance frequencies of interest based on the Dryden turbulence model.

The sensitivity singular values show improved disturbance rejection within the frequency range of interest. The maximum lateral singular values are reduced from 15.6 dB to 7.9 dB, and the longitudinal are reduced from 3.8 dB to 1.0 dB. This indicates that the energy transfer of wind disturbances to the output states of the aircraft may be reduced by adding the inner acceleration feedback loop. To verify this theoretical improvement, MATLAB was used to run nonlinear flight simulations, producing the results presented and discussed next.

The MATLAB simulation applied wind disturbances to the nonlinear aircraft model. The aircraft was initialized in its straight and level flight trim condition, and was buffeted by the wind for 10 seconds with a simulation time step of 1 ms. Both the nominal outer loop controller and the augmented acceleration feedback controller were modeled in separate simulations with the same applied wind velocities. The white noise signal was generated using random seeds produced by MATLAB and sent through Simulink’s Dryden Wind Turbulence Model block to produce the wind

velocities (Figure 5.2).

The resulting longitudinal and lateral states of the aircraft with and without acceleration feedback are shown in Figures 5.3 and 5.4 for both a single simulation run and 100 simulation runs. Each simulation was started with a random white noise seed to produce different wind turbulence signals. The plots for 100 simulations show the shaded range of each state for visibility. The upper and lower bounds of the shaded regions represent the worst-case deviations of the states from trim over all 100 simulations. The acceleration feedback controller produces smoother states with lower magnitudes of oscillations, especially in forward velocity u , pitch rate q , and heading angle ψ .

The acceleration states were also captured by the simulation (Figure 5.5) with translational accelerations are given in m/s^2 and the angular accelerations in rad/s^2 . The acceleration feedback controller greatly reduces the amplitude of the acceleration state oscillations for states \dot{u} , \dot{p} , and \dot{q} . The other three states are largely similar for both controller cases.

The control commands are presented in Figure 5.6. The controller with acceleration feedback produces larger amplitudes and more oscillations in the control signals than the nominal case to compensate for the wind-induced accelerations. The effect is especially pronounced in the rudder signal, which oscillates over its full range of $\pm 45^\circ$ even with the reduced weighting of δ_r in the inner loop control matrix K_i as discussed in section 4.3.

The results were analyzed by calculating the standard deviation of the error signal (difference from the trim condition) for each aircraft state in each simulation run. The error standard deviations were averaged over all 100 simulation runs to produce the results in Table 5.1. The error standard deviation results match the intuition provided by the previous state time-history plots. The forward velocity and acceleration, pitch rate and acceleration, roll acceleration, and heading angle have improvements equal to or greater than 28% considering the error standard deviations. Other states including height, lateral acceleration, roll angle and rate, and yaw rate and acceleration have between 10 and 20% improvement with acceleration feedback. The velocity states v and w show little to no improvement over the nominal controller case. This is likely because the control inputs of the aircraft do not directly affect these states. On a fixed-wing platform, the lateral velocity

v is indirectly altered through steering with roll and yaw, and the heave velocity w is altered by changing forward speed and pitch to produce lift.

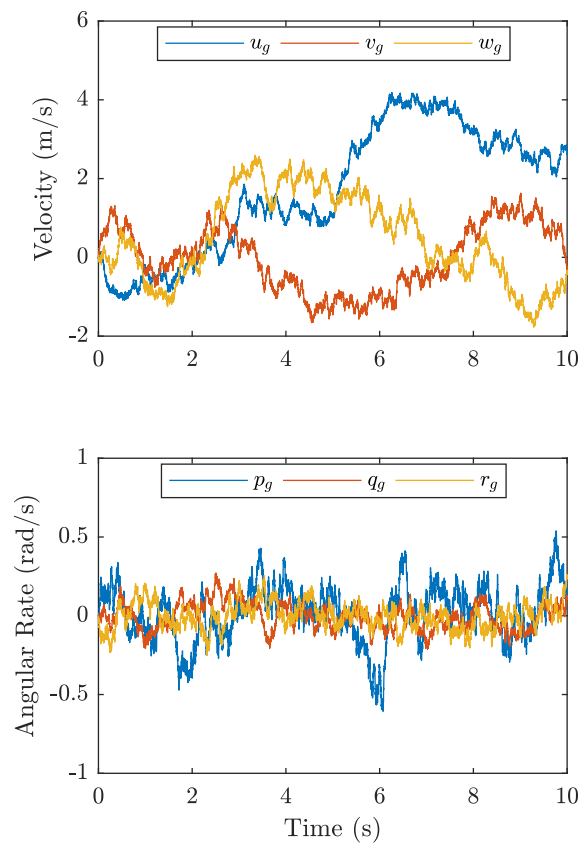


Figure 5.2: Simulated Dryden wind velocities.

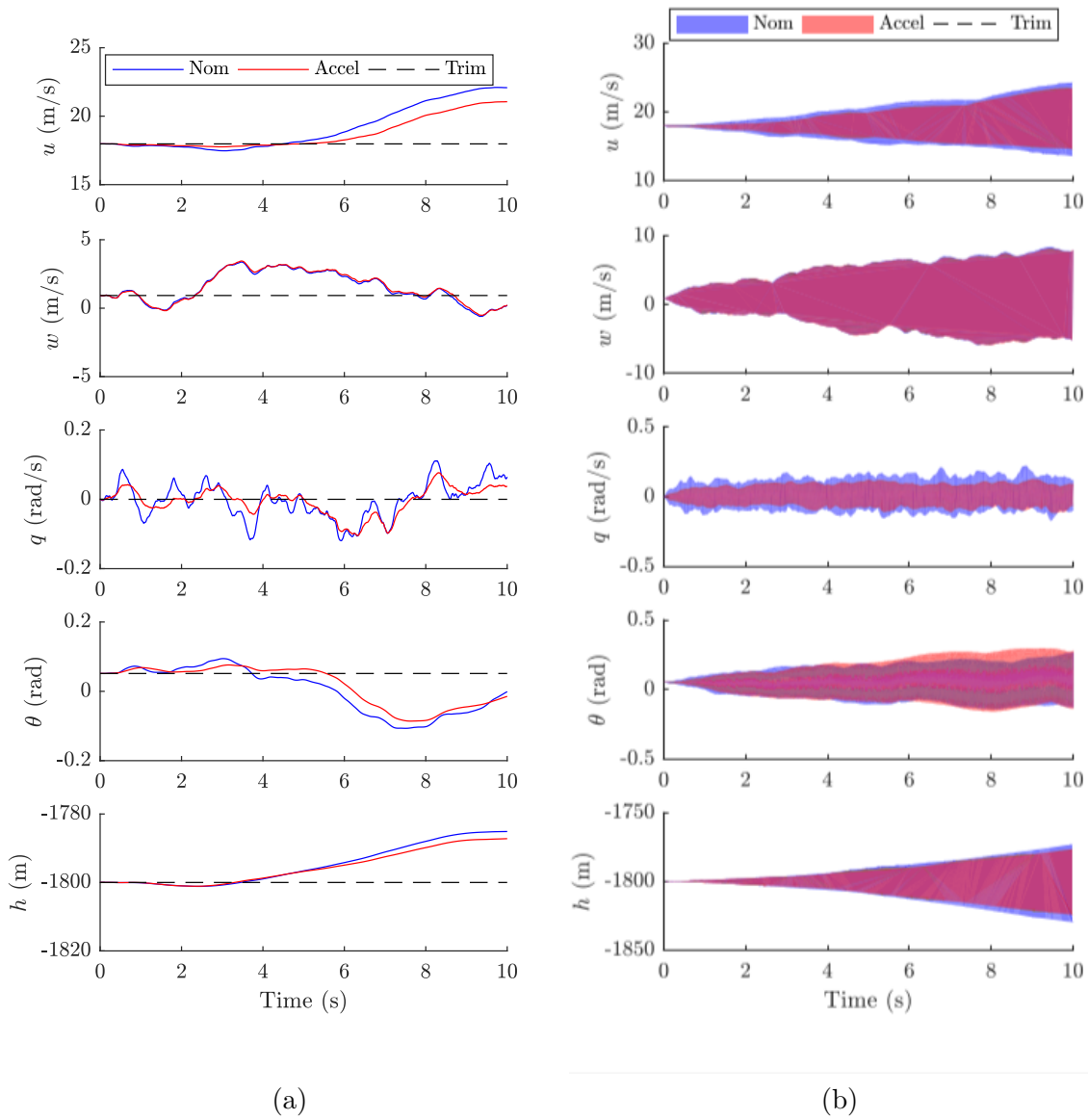


Figure 5.3: Time histories of longitudinal states from nonlinear simulations with each controller, for (a) 1 simulation and (b) shaded ranges for 100 simulations.

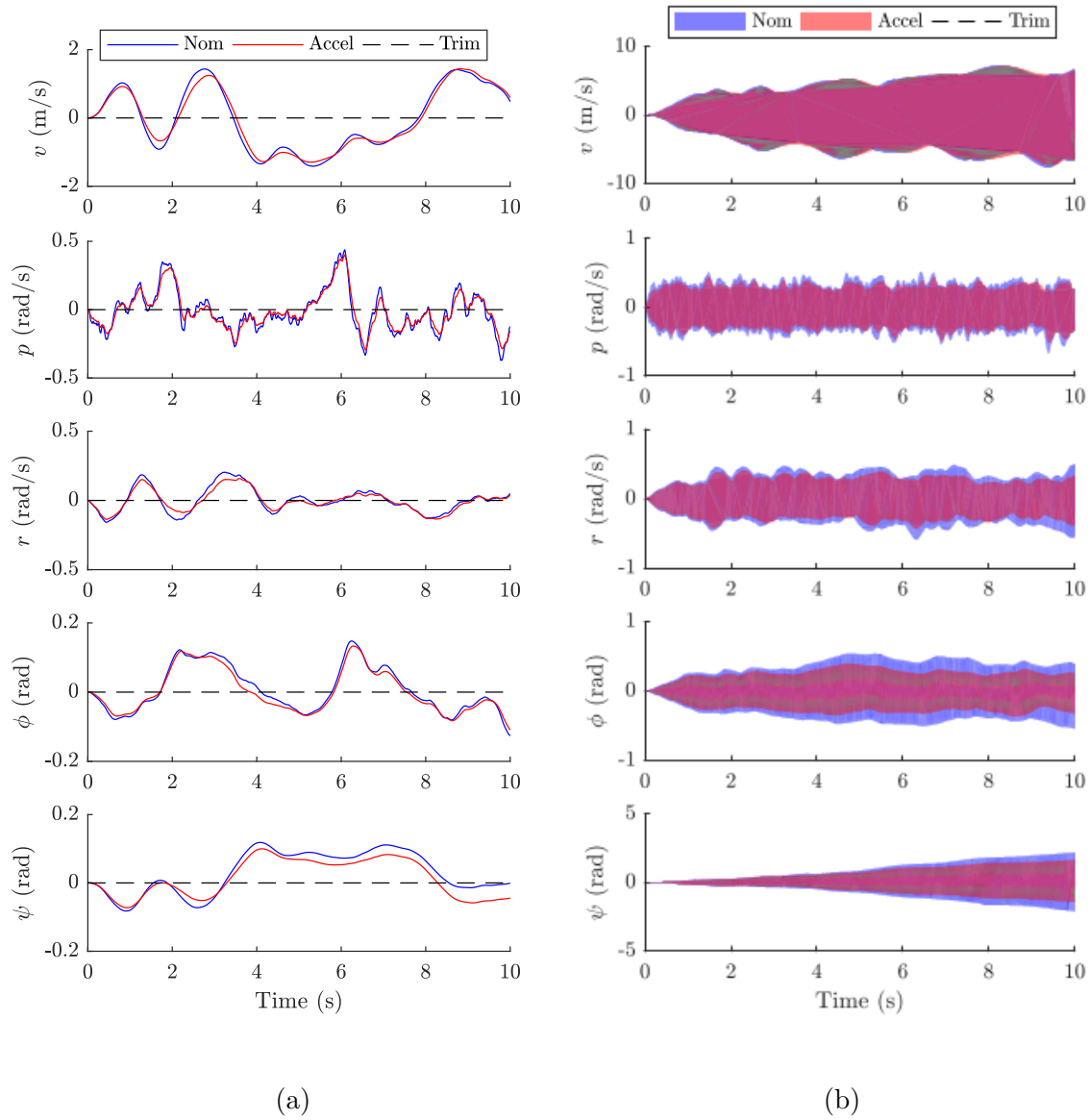


Figure 5.4: Time histories of lateral states from nonlinear simulations with each controller, for (a) 1 simulation and (b) shaded ranges for 100 simulations.

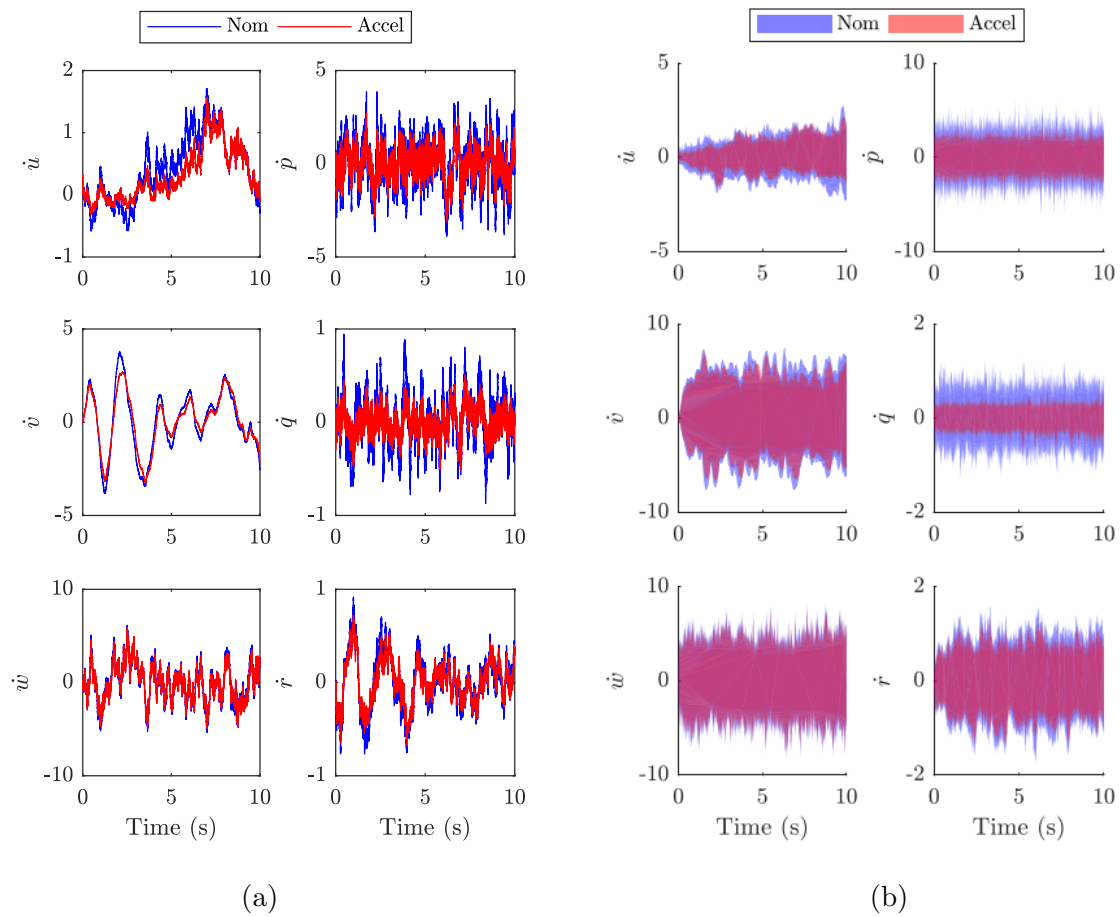


Figure 5.5: Time histories of acceleration states from nonlinear simulations with each controller, for (a) 1 simulation and (b) shaded ranges for 100 simulations.

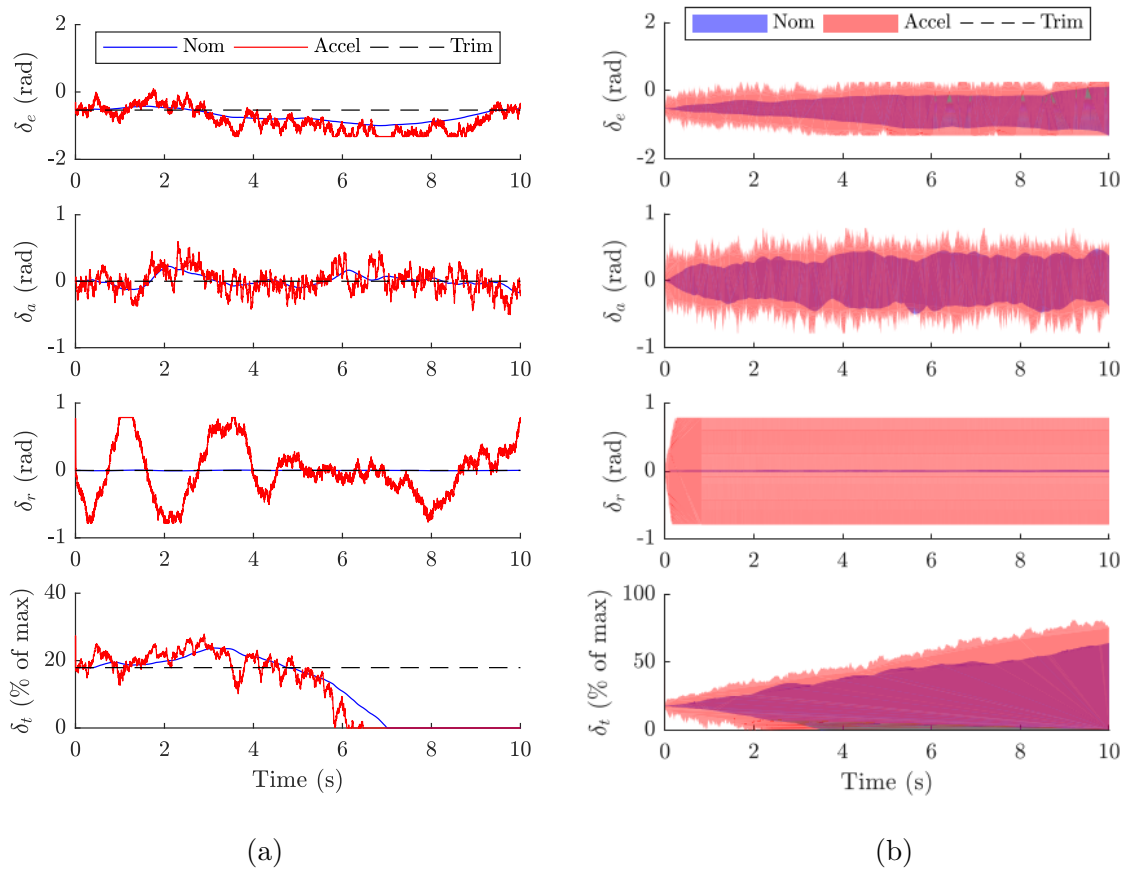


Figure 5.6: Time histories of control inputs from nonlinear simulations with each controller, for (a) 1 simulation and (b) shaded ranges for 100 simulations.

Table 5.1: Nominal and acceleration feedback performance of wind disturbance rejection.

Controller	Error Standard Deviation $\sigma(e)$							
	u (m/s)	w (m/s)	q (rad/s)	θ (rad)	h (m)	\dot{u} (m/s ²)	\dot{w} (m/s ²)	\dot{q} (rad/s ²)
Nominal	0.622	1.129	0.045	0.036	3.552	0.431	1.981	0.290
Acceleration Feedback	0.418	1.134	0.030	0.035	2.972	0.272	1.822	0.121
Improvement (%)	33	-0.4	34	3.5	16	37	8.0	58
	v (m/s)	p (rad/s)	r (rad/s)	ϕ (rad)	ψ (rad)	\dot{v} (m/s ²)	\dot{p} (rad/s ²)	\dot{r} (rad/s ²)
Nominal	1.182	0.144	0.119	0.096	0.200	1.981	1.328	0.389
Acceleration Feedback	1.141	0.126	0.098	0.078	0.144	1.658	0.873	0.309
Improvement (%)	3.5	13	17	19	28	16	34	20

The resulting trajectories of the aircraft with and without acceleration feedback are shown in Figure 5.7 for both a single simulation run and 100 simulation runs. The final lateral deviation from the straight-and-level path is reduced by over 50% by acceleration feedback in the single simulation run. The aircraft’s position drifts with both controllers because the wind velocities have nonzero mean, and the controllers do not correct position error. The addition of a higher-level path planning and position-correcting loop around each stabilizing controller would cause both to stay closer to the desired trajectory, and the acceleration feedback controller would further reduce deviations.

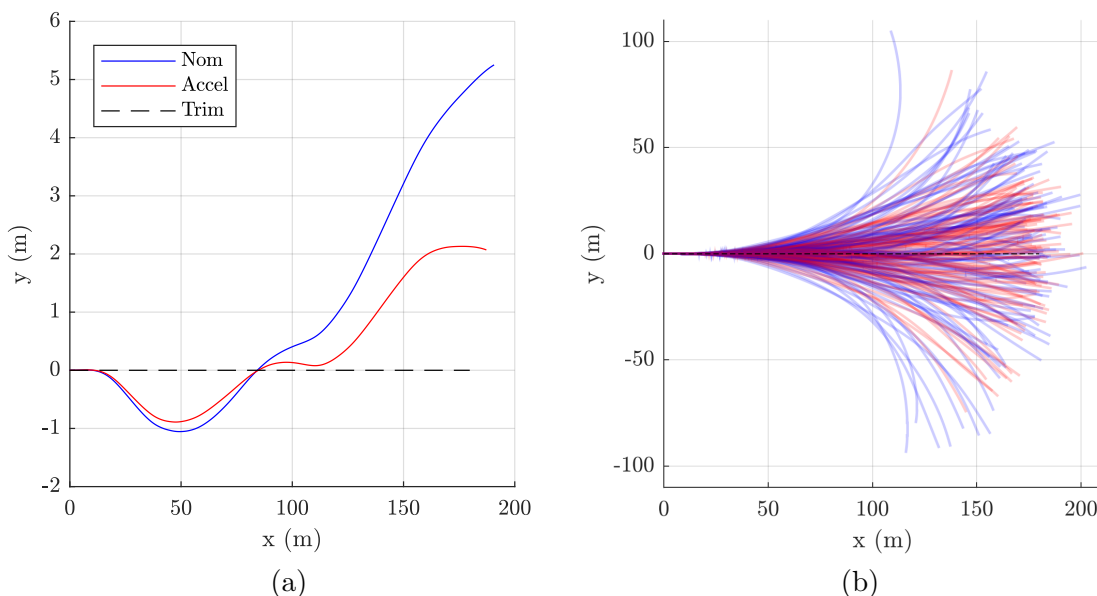


Figure 5.7: Trajectories of the aircraft with each controller, compared to straight trim trajectory, for (a) 1 simulation and (b) 100 simulations.

5.3 Noise Sensitivity

The sensitivity of the acceleration feedback closed loop to sensor noise should be identified. Figure 5.8 displays the location of additive accelerometer noise in the block diagram of the closed loop system. Assuming additive sensor noise in the acceleration states, the transfer function from noise \mathbf{n} to outputs \mathbf{y} can be found by adjusting the control input \mathbf{u} equation to include the noise

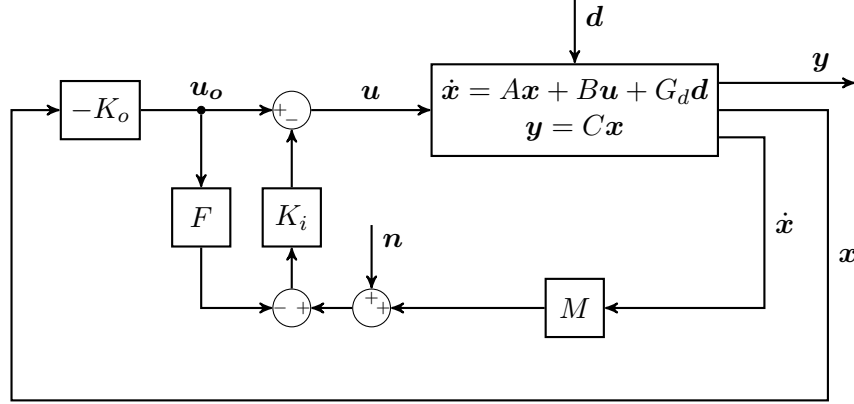


Figure 5.8: Acceleration feedback control block diagram with additive sensor noise at the acceleration states.

vector

$$\begin{aligned}
 \mathbf{u} &= -K_o \mathbf{x} - K_i (M \mathbf{s} \mathbf{x} + n + F K_o \mathbf{x}) \\
 &= -(K_o + K_i M s + K_i F K_o) \mathbf{x} - K_i \mathbf{n} \\
 &= -K_e \mathbf{x} - K_i \mathbf{n}
 \end{aligned} \tag{5.6}$$

This input is substituted in the state-space equations $\dot{\mathbf{x}} = A\mathbf{x} + B\mathbf{u}$ and $\mathbf{y} = C\mathbf{x}$ to produce

$$\begin{aligned}
 \mathbf{y} &= C\mathbf{x} \\
 \mathbf{y} &= C(sI - A + BK_e)^{-1} (-BK_i \mathbf{n})
 \end{aligned} \tag{5.7}$$

Thus, the noise sensitivity transfer function NS from noise to outputs is formed using the definition $\mathbf{y} = NS\mathbf{n}$ as:

$$NS = -C(sI - A + BK_e)^{-1} BK_i \tag{5.8}$$

The maximum singular values of the noise sensitivity function characterize the response of the system to additive sensor noise over frequency. It is desired for the singular values to be low at higher frequencies at which accelerometer noise will occur. Figure 5.9 indicates that the high-

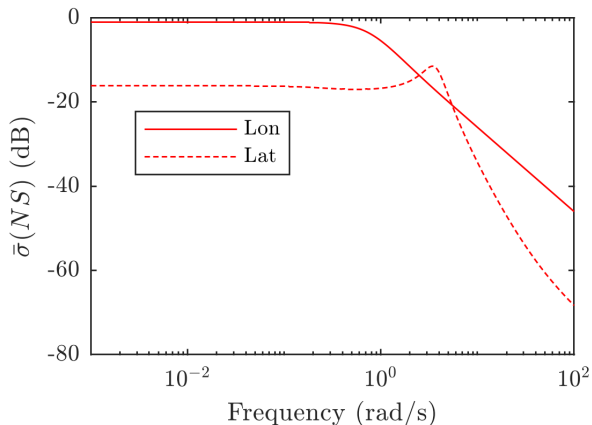


Figure 5.9: Noise rejection singular values for the acceleration feedback controller, in longitudinal (solid) and lateral (dashed) directions.

frequency sensor noise will be attenuated at the outputs of the system.

5.4 Conclusions

In this chapter, the performance of an acceleration feedback controller was compared to a nominal controller through transfer function analysis and nonlinear simulation. The closed-loop system's sensitivity to output disturbances was reduced by the acceleration feedback augmentation for low frequencies within the range of most wind turbulence (less than 1 rad/s). The sensitivity of the acceleration feedback controller to noise in the acceleration states was also examined to show that the effect of sensor noise would drop off at high frequencies.

Disturbance rejection performance was improved in a nonlinear simulation with Dryden turbulence. The improvement was significant only in some aircraft states, most notably in longitudinal directions. For fixed-wing vehicles, stabilization of the longitudinal states is more important to ensure lift; fixed-wing vehicles are thus designed to be more maneuverable in longitudinal states. The velocity states that showed the most improvement with acceleration feedback were the forward velocity u and pitch rate q , by 33% and 34%, respectively. This indicates an increased capability for flight stabilization of fixed-wing vehicles even in turbulent environments. However, the disturbance rejection performance was limited in the lateral directions by the aircraft's inability to respond

to lateral control inputs. Disturbance rejection in the lateral directions was especially limited for the Ttwistor aircraft model in this work because it was less responsive to lateral control inputs as shown by the maneuverability analysis in section 3.2. The rudder control surface was commanded with over 10 times larger amplitude in the acceleration feedback case, but provided relatively low improvement (17%) in yaw rate disturbance rejection.

The heave and lateral velocity disturbance directions (w and v) were also difficult to reject and produced less than 5% improvement with acceleration feedback (with the w state showing decreased performance by -0.4%). This is also a product of the typical fixed-wing control configuration. The common elevator, aileron, rudder, and throttle configuration allows the aircraft to most directly change its pitch, roll, yaw, and forward velocity, but other states (such as heave and lateral velocities) are only impacted indirectly through the other states. The Ttwistor linear model's B matrices in Chapter 2 and maneuverability analysis in Chapter 3 support this lack of control authority; the reachability ellipsoid is shorter in v and w directions.

Another important note is that the augmented controller produced larger actuator commands than the nominal case. In hardware implementation, fixed-wing actuators have saturation and speed limits similar to those modeled in this work. If the controller is improperly designed, the inner loop may cause actuator saturation leading to poor performance. As a result, the outer loop controller design must impose stricter control effort restrictions to account for the additional control input commands of acceleration feedback. The results of the performance assessment in this chapter illustrated the limitations of the acceleration feedback control approach with fixed-wing vehicles, and the need for maneuverability assessment of bare airframes prior to implementation. The maneuverability and gust sensitivity analyses presented in Chapter 3 should be used to determine aircraft candidacy for acceleration feedback control.

Chapter 6

Summary and Future Work

6.1 Summary

This thesis outlined the need for control schemes to enable small UAS to fly through highly turbulent environments in Chapter 1. Inspired by insect flight, distributed sensing and force-and-moment feedback control methods provide the potential for more robust flight especially for small platforms with size, weight and power constraints. Distributed accelerometers can be used to estimate and feed back acceleration states in an inner loop to augment existing aircraft controllers. This method allows disturbances to be sensed and corrected as soon as they exert a force on the vehicle, instead of being fed back in position and velocity states after they have caused vehicle motion.

In Chapter 2, the UAS and environment models used for performance analysis were outlined. The linear and nonlinear models of the Ttwistor UAS and the Dryden turbulence model for wind disturbances were explained. This led to the aircraft candidacy assessment in Chapter 3, which provided maneuverability and gust sensitivity analysis tools to determine whether a bare airframe would be a good candidate for augmented control. High sensitivity to gusts and high maneuverability were factors for good candidacy.

Chapter 4 described the acceleration feedback control scheme as well as the nominal outer loop controller used for comparison. The outer loop LQR controller and inner loop acceleration feedback controllers were designed for the Ttwistor UAS. We outlined the distributed accelerometer equations for linearly estimating acceleration states, and augmented them for a fixed-wing vehicle in

forward flight. Improved gust rejection was demonstrated in Chapter 5 with acceleration feedback on a 6 degree-of-freedom fixed-wing system using both linear model analysis and a nonlinear flight simulation. The singular values of sensitivity transfer functions indicated sufficient attenuation of high-frequency accelerometer noise and improved disturbance rejection performance within the bandwidth of most turbulence. Simulation results showed significant improvement in disturbance rejection performance for some states (up to 58%) with the addition of an acceleration feedback loop to a nominal full-state-feedback controller. The magnitudes of some of the aircraft states in response to moderate turbulence were reduced, and as a result the simulated aircraft flew closer to its desired trajectory. However, the disturbance rejection performance was limited by the maneuverability of the chosen aircraft model, motivating the maneuverability analysis in Chapter 3. We speculated there would be potential for more improvement with a smaller, more agile aircraft.

6.2 Future Work

For future directions, a simulation using a smaller, more responsive fixed-wing aircraft model is recommended. The MATLAB simulation developed in this work can be easily modified to utilize different aircraft models, and the wind model may be augmented to include discrete gusts and wind shear, which would further test the capabilities of the acceleration feedback controller by introducing larger disturbances with more frequency content. In addition, we propose analysis of the controller's performance for disturbances occurring at the plant input, output, or directly as forces and moments.

The performance of the acceleration feedback controller in the presence of model uncertainties has not been explored. In the future, the robust stability and performance of the closed-loop system with this control methodology should be assessed.

There is also a potential for other acceleration estimation schemes than the one proposed in section 4.4. The translational velocities of the vehicle could be estimated using Kalman-filtered IMU data instead of assuming trim values. New methods should be explored and estimation error compared.

This work suggests that acceleration feedback may provide small fixed-wing vehicles with greater flight stability and disturbance rejection in the presence of environmental uncertainties and wind turbulence. Future work should lead to implementation of acceleration feedback with fixed-wing UAS hardware to illustrate the capabilities of this control method in uncertain, gusty real-world environments. Eventual implementations may be miniaturized for use on insect-scale vehicles to enable robust flight at smaller scales.

Bibliography

- [1] ADXL325 Datasheet and Product Info.
- [2] Analog Devices Gyroscopes.
- [3] MIL-HDBK-1797 - Flying Qualities of Piloted Aircraft. U.S. Department of Defense, December 1997.
- [4] Simulink Documentation, 2018.
- [5] Sweta Agrawal, David Grimaldi, and Jessica L. Fox. Haltere morphology and campaniform sensilla arrangement across Diptera. Arthropod Structure & Development, 46(2):215–229, March 2017.
- [6] M. Ahsan, H. Rafique, and Z. Abbas. Heading control of a fixed wing UAV using alternate control surfaces. In 2012 15th International Multitopic Conference (INMIC), pages 125–129, December 2012.
- [7] M. Ahsan, K. Shafique, A. B. Mansoor, and M. Mushtaq. Performance comparison of two altitude-control algorithms for a fixed-wing UAV. In 2013 3rd IEEE International Conference on Computer, Control and Communication (IC4), pages 1–5, September 2013.
- [8] Seyma Akyurek, Unver Kaynak, and Coku Kasnakolu. Altitude Control for Small Fixed-Wing Aircraft Using H Loop-Shaping Method. IFAC-PapersOnLine, 49(9):111–116, January 2016.
- [9] Barton J. Bacon and Aaron J. Ostroff. Reconfigurable Flight Control Using Nonlinear Dynamic Inversion with a Special Accelerometer Implementation. Technical Report AIAA-2000-4565, NASA Langley Research Center, 2000.
- [10] Randal Beard and Timothy McLain. Small Unmanned Aircraft: Theory and Practice. Princeton University Press, 2012.
- [11] Lina Castano, Simone Airoidi, Terrence McKenna, and James Humbert. Gust rejection using force adaptive feedback for roll. In 14th AIAA Aviation Technology, Integration, and Operations Conference. American Institute of Aeronautics and Astronautics, June 2014.
- [12] Lina Castano, Simone Airoidi, Terrence McKenna, and James Humbert. Wing Sensor Placement for Gust Disturbance Rejection. In AIAA Atmospheric Flight Mechanics Conference. American Institute of Aeronautics and Astronautics, 2015.

- [13] May Chan. Integration of Macro-Fiber Composite Material on a Low Cost Unmanned Aerial System. Master of Science in Aerospace Engineering, Embry-Riddle Aeronautical University, May 2017.
- [14] H. Chao, Y. Cao, and Y. Chen. Autopilots for Small Fixed-Wing Unmanned Air Vehicles: A Survey. In 2007 International Conference on Mechatronics and Automation, pages 3144–3149, August 2007.
- [15] H. B. Chen and S. G. Zhang. Robust dynamic inversion flight control law design. In 2008 2nd International Symposium on Systems and Control in Aerospace and Astronautics, pages 1–6, December 2008.
- [16] Jeng-Heng Chen, Sou-Chen Lee, and Daniel DeBra. Gyroscope Free Strapdown Inertial Measurement Unit by Six Linear Accelerometers. Journal of Guidance, Control, and Dynamics, 17(2):286–290, April 1994.
- [17] Grace A. Clark. Angular and Linear Velocity Estimation for a Re-Entry Vehicle Using Six Distributed Accelerometers: Theory. Lawrence Livermore National Lab., Technical Rept. UCRL-ID-153253, Livermore, CA, 2003.
- [18] John L. Crassidis and John L. Junkins. Optimal Estimation of Dynamic Systems. CRC Press, Boca Raton, FL, 2 edition, 2011.
- [19] William Derham. Physico-theology : or, a demonstration of the being and attributes of God, from his works of creation : being the substance of sixteen sermons preached in St. Mary-le-Bow-Church, London, at the honourable Mr. Boyle’s lectures in the years 1711, and 1712 ... London : Printed for W. and J. Innys, 1720.
- [20] Renee C. Gardner and J. Sean Humbert. Comparative Framework for Maneuverability and Gust Tolerance of Microhelicopters. Journal of Aircraft, 51(5):1546–1553, 2014.
- [21] W. E. Green and P. Y. Oh. A MAV that flies like an airplane and hovers like a helicopter. In Proceedings, 2005 IEEE/ASME International Conference on Advanced Intelligent Mechatronics., pages 693–698, July 2005.
- [22] Gregory M. Gremillion, Lina Castano, and James Humbert. Disturbance Rejection with Distributed Acceleration and Strain Sensing. In AIAA Guidance, Navigation, and Control Conference. American Institute of Aeronautics and Astronautics, 2015.
- [23] Gregory M. Gremillion and J. Sean Humbert. Disturbance Rejection with Distributed Acceleration Sensing for Small Unmanned Aircraft Systems. AIAA Journal, 54(8):2233–2246, 2016.
- [24] Y. Q. He and J. D. Han. Acceleration-Feedback-Enhanced Robust Control of an Unmanned Helicopter. Journal of Guidance, Control, and Dynamics, 33(4):1236–1250, 2010.
- [25] Coku Kasnakolu. Investigation of Multi-Input Multi-Output Robust Control Methods to Handle Parametric Uncertainties in Autopilot Design. PLOS ONE, 11(10):e0165017, October 2016.

- [26] L. Keviczky and C. Bnysz. MIMO controller design for decoupling aircraft lateral dynamics. In 2011 9th IEEE International Conference on Control and Automation (ICCA), pages 1079–1084, 2011.
- [27] S. Leven, J. C. Zufferey, and D. Floreano. A minimalist control strategy for small UAVs. In 2009 IEEE/RSJ International Conference on Intelligent Robots and Systems, pages 2873–2878, October 2009.
- [28] Jerry M. Mendel. Lessons in Estimation Theory for Signal Processing, Communications, and Control. Prentice Hall, Upper Saddle River, NJ, 1995.
- [29] Bernard Michini. Modeling and Adaptive Control of Indoor Unmanned Aerial Vehicles. PhD thesis, Massachusetts Institute of Technology, September 2009.
- [30] Mehran Motamed and J. Yan. A review of biological, biomimetic and miniature force sensing for microflight. In 2005 IEEE/RSJ International Conference on Intelligent Robots and Systems, pages 3939–3946, August 2005.
- [31] Jason Roadman, Jack Elston, Brian Argrow, and Eric Frew. Mission Performance of the Tempest Unmanned Aircraft System in Supercell Storms. Journal of Aircraft, 49(6):1821–1830, November 2012.
- [32] H. S. Shin, L. M. Castano, J. S. Humbert, and S. Bergbreiter. Sensing skin for detecting wing deformation with embedded soft strain sensors. In 2016 IEEE SENSORS, pages 1–3, October 2016.
- [33] P. Simplicio, M. D. Pavel, E. van Kampen, and Q. P. Chu. An acceleration measurements-based approach for helicopter nonlinear flight control using Incremental Nonlinear Dynamic Inversion. Control Engineering Practice, 21(8):1065–1077, August 2013.
- [34] Sigurd Skogestad and Ian Postlethwaite. Multivariable Feedback Control: Analysis and Design. John Wiley & Sons, Inc., Chichester. New York. Brisbane. Toronto. Singapore, 2 edition, August 2001.
- [35] Brian Stevens and Frank Lewis. Aircraft Control and Simulation. John Wiley & Sons, Inc., 2 edition, 2003.
- [36] Peter M. Thompson, Amanda K. Lampton, Richard C. Lind, and Rhoe A. Thompson. Attitude Control Enhancement for Small and Micro Air Vehicles Using Acceleration Feedback. In AIAA Atmospheric Flight Mechanics (AFM) Conference, Boston, MA, August 2013. American Institute of Aeronautics and Astronautics.
- [37] Rhoe Thompson, Johnny Evers, and Kelly Stewart. Attitude Control Augmentation Using Wing Load Sensing - A Biologically Motivated Strategy. In Guidance, Navigation, and Control and Co-located Conferences, Toronto, Ontario Canada, August 2010. American Institute of Aeronautics and Astronautics.
- [38] Julian F. V. Vincent, Sally E. Clift, and Carlo Menon. Biomimetics of Campaniform Sensilla: Measuring Strain from the Deformation of Holes. Journal of Bionic Engineering, 4(2):63–76, June 2007.

- [39] R. J. Wood and R. S. Fearing. Flight force measurements for a micromechanical flying insect. In Proceedings 2001 IEEE/RSJ International Conference on Intelligent Robots and Systems. Expanding the Societal Role of Robotics in the the Next Millennium (Cat. No.01CH37180), volume 1, pages 355–362 vol.1, 2001.
- [40] Ruiyong Zhai, Zhaoying Zhou, Wendong Zhang, Shengbo Sang, and Pengwei Li. Control and navigation system for a fixed-wing unmanned aerial vehicle. AIP Advances, 4(3):031306, February 2014.
- [41] Kemin Zhou, Gregory Salomon, and Eva Wu. Balanced realization and model reduction for unstable systems. International Journal of Robust and Nonlinear Control, 9(3):183–198, March 1999.